

Comprehensive nucleosynthesis analysis for ejecta of compact binary mergers

O. Just,^{1,2} A. Bauswein,³ R. Ardevol Pulpillo,^{1,4} S. Goriely⁵ and H.-T. Janka¹

¹*Max-Planck-Institut für Astrophysik, Postfach 1317, 85741 Garching, Germany*

²*Max-Planck/Princeton Center for Plasma Physics (MPPC)*

³*Department of Physics, Aristotle University of Thessaloniki, 54124 Thessaloniki, Greece*

⁴*Physik Department, Technische Universität München, James-Frank-Straße 1, 85748 Garching, Germany*

⁵*Institut d’Astronomie et d’Astrophysique, CP-226, Université Libre de Bruxelles, 1050 Brussels, Belgium*

Released 2014 Xxxxx XX

ABSTRACT

We present the first comprehensive study of r-process element nucleosynthesis in the ejecta of compact binary mergers (CBMs) and their relic black-hole (BH)-torus systems. The evolution of the BH-accretion tori is simulated for seconds with a Newtonian hydrodynamics code including viscosity effects, pseudo-Newtonian gravity for rotating BHs, and an energy-dependent two-moment closure scheme for the transport of electron neutrinos and antineutrinos. The investigated cases are guided by relativistic double neutron star (NS-NS) and NS-BH merger models, producing $\sim 3\text{--}6 M_{\odot}$ BHs with rotation parameters of $A_{\text{BH}} \sim 0.8$ and tori of $0.03\text{--}0.3 M_{\odot}$. Our nucleosynthesis analysis includes the dynamical (prompt) ejecta expelled during the CBM phase and the neutrino and viscously driven outflows of the relic BH-torus systems. While typically $\sim 20\text{--}25\%$ of the initial accretion-torus mass are lost by viscously driven outflows, neutrino-powered winds contribute at most another $\sim 1\%$, but neutrino heating enhances the viscous ejecta significantly. Since BH-torus ejecta possess a wide distribution of electron fractions ($0.1\text{--}0.6$) and entropies, they produce heavy elements from $A \sim 80$ up to the actinides, with relative contributions of $A \gtrsim 130$ nuclei being subdominant and sensitively dependent on BH and torus masses and the exact treatment of shear viscosity. The combined ejecta of CBM and BH-torus phases can reproduce the solar abundances amazingly well for $A \gtrsim 90$. Varying contributions of the torus ejecta might account for observed variations of lighter elements with $40 \leq Z \leq 56$ relative to heavier ones, and a considerable reduction of the prompt ejecta compared to the torus ejecta, e.g. in highly asymmetric NS-BH mergers, might explain the composition of heavy-element deficient stars.

Key words: nuclear reactions, nucleosynthesis, abundances – hydrodynamics – neutrinos – accretion, accretion discs – stars: neutron – stars: black holes

1 INTRODUCTION

Double neutron star (NS-NS) and neutron star-black hole (NS-BH) binaries radiate gravitational waves and their orbits shrink due to the associated angular momentum and energy loss until, after millions to hundreds of millions of years, a catastrophic merger event terminates the evolution of these binary systems. The frequency of such events can be estimated on grounds of the known double NS systems in the solar neighborhood (e.g., Kalogera et al. 2004) and theoretical population synthesis studies (e.g., Belczynski et al. 2008) to be of the order of one NS-NS merger in some 10^5 years for Milky Way-like galaxies and possibly up to several times this rate for NS-BH mergers, but these numbers contain considerable uncertainties (Postnov & Yungelson 2014).

Compact binary mergers are among the most promising extragalactic sources of gravitational waves (GWs) in the $\lesssim 100$ to $\gtrsim 1000$ Hz range to be measured by the upcoming advanced interferometer antennas (advLIGO, advVIRGO, KAGRA). Strong arguments suggest that their remnants are good candidates for the still enigmatic central engines of short gamma-ray bursts (GRBs; see, e.g., Berger 2014; Nakar 2007 for reviews). The merger rate, reduced by the beaming factor measuring the probability that the Earth is hit by the collimated, ultrarelativistic GRB beam, can well account for the number of detected short GRBs.

Moreover, a small fraction of the NS matter can be expelled during and after the coalescence of the binary components. Because of its extremely neutron-rich initial state, this

matter has long been speculated to be a possible site for the formation of r-process nuclei (Lattimer & Schramm 1974, 1976; Eichler et al. 1989). Indeed, Newtonian (e.g., Ruffert et al. 1997; Ruffert & Janka 1999, 2001; Janka et al. 1999; Rosswog et al. 1999; Freiburghaus et al. 1999; Rosswog 2005; Korobkin et al. 2012) and conformally flat general relativistic (e.g., Oechslin et al. 2007; Goriely et al. 2011b; Bauswein et al. 2013b) as well as fully relativistic (e.g., Kyutoku et al. 2011, 2013; Hotokezaka et al. 2013a,b; Deaton et al. 2013; Wanajo et al. 2014; Foucart et al. 2014) hydrodynamical simulations of NS-NS and NS-BH mergers with microphysical equations of state (EOSs) have demonstrated that typically some $10^{-3} M_{\odot}$ up to more than $0.1 M_{\odot}$ can become gravitationally unbound on roughly dynamical timescales due to shock acceleration and tidal stripping. Also the relic object, either a hot, transiently stable hypermassive NS (HMNS; stabilized by differential rotation and thermal pressure; Baumgarte et al. 2000) and later supermassive NS (SMNS; stabilized by rigid rotation and thermal pressure) or a BH-torus system (Fig. 1, upper panel), can lose mass along with its secular evolution in outflows that are driven by viscous energy dissipation and turbulent angular momentum transport, magnetic pressure, nucleon-recombination heating and neutrino-energy deposition (Fig. 1, lower panel; e.g., Popham et al. 1999; Ruffert & Janka 1999; Dessart et al. 2009; Fernández & Metzger 2013; Siegel et al. 2014; Metzger & Fernández 2014; Perego et al. 2014). Such ejecta could be interesting environments for r-process, p-process, and nickel nucleosynthesis (e.g., Surman et al. 2008; Caballero et al. 2012; Wanajo & Janka 2012; Malkus et al. 2014; Surman et al. 2014, and references therein).

The presence of significant mass fractions of radioactive material (nickel, r-nuclei,...) was pointed out to lead to long-term decay heating of the material ejected by compact binary mergers and thus to thermal radiation that can potentially be observed as electromagnetic transient (Li & Paczyński 1998) termed “macro-nova” (Kulkarni 2005) or “kilonova” (Metzger et al. 2010; Metzger & Berger 2012). Indeed, a near-infrared data point at the position of the short-hard GRB 130603B about 7 days (rest-frame time) after the burst was interpreted as possible first detection of such an r-process powered transient (Berger et al. 2013; Tanvir et al. 2013), because its temporal delay, color, and brightness are compatible with theoretical light curve calculations for an assumed ejecta mass of some $10^{-2} M_{\odot}$, taking into account the fact that r-process nuclei, in particular the abundant lanthanides, increase the opacity by roughly a factor of 100 compared to iron (Barnes & Kasen 2013; Kasen et al. 2013; Hotokezaka et al. 2013b; Tanaka & Hotokezaka 2013; Tanaka et al. 2014; Grossman et al. 2014).

Nucleosynthesis calculations agree (e.g., Freiburghaus et al. 1999; Goriely et al. 2005; Roberts et al. 2011; Goriely et al. 2011b; Korobkin et al. 2012; Bauswein et al. 2013b; Rosswog et al. 2014; Wanajo et al. 2014) that the dynamical ejecta of the merging phase provide sufficiently neutron rich conditions for a robust r-processing up to the third abundance peak and the actinides, although the theoretical predictions show considerable differences in important details, depending on the exact conditions in the ejecta (electron fraction, Y_e , expansion velocity, and specific entropy) and the employed nuclear physics, in particular the theoretical assumptions about the fission-fragment distribution

(cf. Goriely et al. 2013). Relativistic NS-NS mergers (e.g., Bauswein et al. 2013b), for example, tend to produce faster ejecta than Newtonian simulations (e.g., Roberts et al. 2011; Korobkin et al. 2012; Rosswog et al. 2014; Grossman et al. 2014), and —compared to models that disregard neutrino effects (e.g., Goriely et al. 2011b; Bauswein et al. 2013b)—, the Y_e in the ejecta is slightly higher when neutrino emission is included (e.g., Korobkin et al. 2012) and could even be significantly higher when neutrino emission and absorption are both taken into account (Wanajo et al. 2014). Slower mass ejection and a wider spread of the neutron excess enable the creation of r-nuclei with mass numbers above $A \sim 80$ –110, whereas fast, very neutron-rich ejecta lead only to species with $A \gtrsim 130$ –140. The exact structure of the second and third peaks as well as the quality of reproducing the solar r-element distribution in the rare-earth region depends sensitively on the nuclear reaction rates and the fission fragment yields, if fission recycling plays an important role. In any case, however, a robust and strong production of lanthanides and third-peak material can be expected.

The hydrodynamics and nucleosynthetic output of merger remnants are less well studied than those of the dynamical merging phase or immediate post-merging phase, mainly because simulations of the evolution of relic massive NSs or BH-torus systems need to be carried out over much longer time intervals. Magnetic fields, turbulence, and viscous effects play important roles and add complications, and a reasonably good treatment of neutrino production, absorption, and transport is indispensable to obtain reliable predictions of the nucleosynthetic conditions in outflows. First interesting modeling attempts of rapidly rotating post-merger HMNSs or SMNSs including a neutrino treatment in two- and three dimensions (2D, 3D) exist (Dessart et al. 2009; Metzger & Fernández 2014; Perego et al. 2014), but the enormous complexity of the problem still enforces considerable simplifications, among them short evolution phases, purely Newtonian gravity, the disregard of magnetic-field effects, simple neutrino treatments, or a parametric, not fully self-consistent description of the neutron-star core as a neutrino emitting boundary irradiating a surrounding disk, or a combination of several of these assumptions.

Hydrodynamical exploration of NS-BH mergers and the early development (over periods of several ten milliseconds) of their relic BH-torus systems has only started to be done in full 3D general relativity with a neutrino-leakage treatment (Deaton et al. 2013; Foucart et al. 2014), but magnetic and viscous effects, which determine the mass-loss of the accretion tori on secular timescales, are still not included in such models. Fernández & Metzger (2013) have recently carried out the first (2D) hydrodynamical simulations of post-merger BH-tori, which were able to follow the long-time evolution over the whole period of intense neutrino emission and a large fraction of the mass-loss history (for many seconds) including an approximative description for neutrino emission and self-irradiation, viscosity terms, and a pseudo-Newtonian treatment of gravity for (nonrotating) BHs following Paczyński & Wiita (1980). This spearheading work went clearly beyond simple parametric or semi-analytic modeling (e.g., Surman et al. 2008; Metzger et al. 2008, 2009; Wanajo & Janka 2012) and earlier (magneto-)hydrodynamical simulations in 2D (Lee et al. 2005; Shibata et al. 2007; Shibata & Sekiguchi 2012; Janiuk

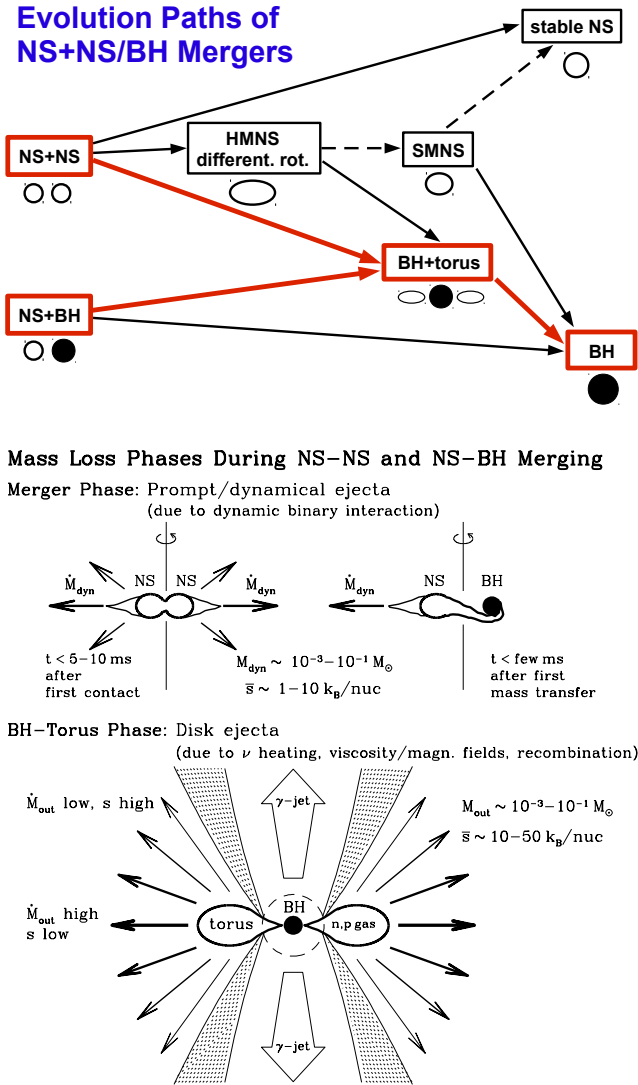


Figure 1. *Top panel:* Evolution paths of NS-NS and NS-BH mergers. Depending on the binary parameters and the properties of the nuclear equation of state, binary NS mergers can lead to the formation of a stable NS, a transient hypermassive NS (HMNS; stabilized by differential rotation) and supermassive NS (SMNS, stabilized by rigid rotation), or a BH plus accretion-torus system. The last scenario is also the outcome of a NS-BH merger if the BH/NS mass ratio is not too large. Transitions between the different evolution stages can be accompanied by mass loss. In the present work we focus exclusively on the evolution tracks and stages highlighted by thick, solid red lines. *Bottom panel:* Mass-loss phases during the dynamical interaction of NS-NS and NS-BH binaries and the subsequent secular evolution of a relic BH-torus system (corresponding to the evolution paths indicated by red lines in the upper panel). The dynamical mass ejection takes place within a few milliseconds when the two binary components merge with each other. Typical ejecta masses are around $0.01 M_{\odot}$ and the average entropies of the ejecta are low. BH-torus systems eject matter mainly in viscously driven outflows and to a smaller extent also in neutrino-driven winds. Baryon-poor polar funnels may provide suitable conditions for neutrino or magnetohydrodynamically powered, ultrarelativistic, collimated outflows, which are likely to produce short gamma-ray bursts. The image is adapted from Ruffert & Janka (1999); Janka & Ruffert (2002).

et al. 2013) and 3D (Ruffert & Janka 1999; Setiawan et al. 2004, 2006). In nucleosynthesis and light-curve calculations of the expanding ejecta of compact binary mergers, however, the contribution from the merger-remnant phase has so far been included only highly schematically, either by applying simple multi-parameter prescriptions for neutrino-driven wind conditions (Rosswog et al. 2014; Grossman et al. 2014) or by making ad hoc assumptions about the composition of the disk-wind ejecta (Barnes & Kasen 2013).

In this work we perform the first comprehensive study of the nucleosynthetic output associated with the ejecta from the merging phase of NS-NS and NS-BH binaries *and* with the neutrino and viscously driven outflows of the subsequent long-time evolution of relic BH-torus systems. The compact binary mergers are simulated with a relativistic smooth-particle-hydrodynamics code (Oechslin et al. 2007; Bauswein 2010) in a conformally flat, dynamical spacetime including temperature-dependent, microphysical EOSs, while the BH-torus modeling is conducted with a Eulerian finite-volume Godunov-type scheme, supplemented by a shear-viscosity treatment with a Shakura-Sunyaev α -prescription for the dynamic viscosity (Shakura & Sunyaev 1973). For the long-time evolution we employ a pseudo-Newtonian approximation of the gravity potential for the rotating relic BHs (Artemova et al. 1996). In the time-dependent BH-torus modeling we apply, for the first time, detailed energy-dependent and velocity-dependent 2D neutrino transport based on a new two-moment closure scheme (Just, Obergaulinger & Janka, in preparation), which allows us to determine the neutrino-driven wind and the neutron-to-proton ratio in the disk outflows with higher accuracy than in previous simulations. All simulations include microphysical treatments of the gas equation of state.

Our nucleosynthesis calculations are carried out in a post-processing step of the ejecta produced by the hydrodynamical models, using a full r-process network including all relevant nuclear reactions (Goriely et al. 2008, 2010; Xu et al. 2013). For the combined analysis we pick cases from larger sets of NS-NS merger models, which lead to prompt or slightly delayed BH formation, and NS-BH merger models on the one side and BH-torus models on the other side such that the macroscopic system parameters (BH and torus masses and BH spins of the merger remnants) match roughly on both sides. This also yields good consistency of the mean values of the total specific energies of the torus gas in both modeling approaches.

We find that the torus outflows complement the dynamical merger ejecta by contributing the lower-mass r-process nuclei ($A \lesssim 140$) that are massively underproduced by the strong r-process taking place in the very neutron-rich material expelled during the binary coalescence. The combined abundance distribution can reproduce the solar pattern amazingly closely, but in contrast to the robustness of the high-mass number component ($A \gtrsim 140$) the low-mass number component must be expected to exhibit considerable variability, depending on the variations of the intrinsic outflow properties. On the other hand, direction-dependent differences result from the combination of highly asymmetric dynamical NS-BH merger ejecta with much more isotropically distributed torus outflows. Cases with suppressed dynamical ejecta component resemble abundance patterns observed in heavy r-element deficient metal-poor stars.

Our paper is structured as follows. In Sect. 2 we briefly summarize the basic methodical aspects of our hydrodynamical modeling of the different considered scenarios and evolution stages and of our nucleosynthesis analysis. In Sect. 3 we describe the conceptual aspects of the coherent modeling approach and present our results for the hydrodynamical simulations of binary mergers and relic BH-torus systems and for the corresponding r-process nucleosynthesis. Section 5 concludes with a summary and discussion of our results. In Appendix A we present a comparison test of our neutrino-transport treatment and briefly discuss the accuracy of the latter.

2 NUMERICAL METHODS

2.1 Compact binary mergers

The merging phase of our models is simulated with a smooth-particle-hydrodynamics (SPH) code with an approximate treatment of relativistic gravity. The code computes the hydrodynamical properties of fluid elements co-moving with the matter flow (see Oechslin et al. 2002, 2007; Bauswein et al. 2010; Bauswein 2010 for details). The Lagrangian nature of this scheme is well suited to follow the unbound material during the coalescence. The relativistic Lagrangian formulation of hydrodynamics evolves so-called “conserved variables”, which yields ordinary differential equations for the conserved rest-mass density ρ^* , the conserved specific momenta \tilde{u}_i and the conserved energy density τ (Siegler & Riffert 2000). The quantities depend on the rest-mass density ρ , the coordinate velocity v_i , the specific internal energy density ϵ , the pressure P , and the metric functions encoding the gravitational field.

The Einstein equations are solved by imposing a conformal flatness condition (CFC) for the spatial metric $ds^2 = -\alpha^2 dt^2 + \psi^4 \delta_{ij} (dx^i + \beta^i dt)(dx^j + \beta^j dt)$, which results in non-linear elliptical equations for the lapse function α , the shift vector β_i and the conformal factor ψ (Isenberg & Nester 1980; Wilson et al. 1996). In the case of NS-NS mergers this CFC approximation has been shown to yield quantitatively accurate results for the oscillation modes of NS-merger remnants and for the properties of ejecta when compared to calculations solving the full Einstein equations (Bauswein et al. 2012, 2013b; Hotokezaka et al. 2013a; Takami et al. 2014).

For the simulation of NS-BH mergers we use the extended CFC formulation (Bonazzola et al. 2004; Cordero-Carrión et al. 2009) to avoid divergence problems in the source terms in the proximity of the BH. In this formulation a BH can be treated by means of the puncture approach (Brandt & Brügmann 1997), which factors out divergent terms in the metric function and which calculates the deviations of the spacetime from a static BH solution, the latter of which is analytically known. In a similar manner the BH momentum and spin are taken into account by adding analytically known solutions to the extrinsic curvature (Bowen 1979; Bowen & York 1980; Bauswein 2010), which appears in the source terms of the elliptical equations. This procedure is fully equivalent to the construction of BH-BH or NS-BH binary initial data necessary for fully relativistic calculations (see e.g. Kyutoku et al. 2009;

Bauswein 2010; Baumgarte & Shapiro 2010, where the corresponding formulae can be found; see also Faber et al. 2006 for a similar approach within CFC). In our implementation, however, the method for computing initial data is employed in every time step (Bauswein 2010). In fully relativistic formulations of the Einstein evolution equations the BH position is tracked passively by $dx_{\text{BH}}^i/dt = -\beta^i(x_{\text{BH}}^i)$ with x_{BH}^i being the center of the BH (position of the puncture). For our calculations we promote this equation to an active equation of motion for the BH to be solved in parallel with the hydrodynamical equations. For details of the implementation, see Bauswein et al. (2010). More information will be provided in a forthcoming paper.

The BH treatment is validated by computing orbits of NS-BH binaries and comparing the orbital angular velocity with stationary calculations of quasi-equilibrium initial data (Etienne et al. 2009), which can be reproduced within a few per cent (Bauswein 2010). More importantly for the purposes of this paper, we also compare the resulting tori of NS-BH mergers with those computed by grid-based fully relativistic simulations (Kyutoku et al. 2011, 2013). Torus masses agree with an accuracy of about 20 per cent for binaries with initially non-rotating as well as rotating BHs. Also the amount of dynamically ejected matter is consistent within a factor of two. We confirm by convergence tests that the torus and ejecta masses are insensitive to the chosen grid setup for the metric solver and the SPH particle resolution within a range of 20 per cent and 30 per cent, respectively.

For NS-BH as well as NS-NS mergers the hydrodynamical equations are supplemented by an additional equation $dY_e/dt = 0$, which describes the advection of the initial electron fraction Y_e . The electron fraction, Y_e , rest-mass density, ρ , and specific internal energy density, ϵ , are employed to call the equation of state (EOS) $P(\rho, \epsilon, Y_e)$, which is required to close the system of hydrodynamical equations. Throughout the paper we use fully temperature-dependent, microphysical high-density equations of state (see Sect. 3.1), which are indispensable for an accurate description of the merger dynamics and a reliable determination of torus and ejecta properties (Bauswein et al. 2010, 2013b). Moreover, the temperature and composition of the ejected material are needed as input to the nucleosynthesis calculations. For NS-NS and NS-BH mergers the NSs are assumed to be initially cold and in neutrinoless β -equilibrium, which sets the initial electron fraction. The stars are placed on circular quasi-equilibrium orbits such that the binaries merge after about two to three revolutions. For both types of systems we impose an initially non-rotating velocity profile of the NSs, because NS spin periods are long compared to the orbital periods and because tidally locked systems are not expected to form during the inspiral (Kochanek 1992; Bildsten & Cutler 1992). The initial rotation of the BH, $A_{\text{BH},0}$, is a free parameter of our setups (see Sect. 3.1). The NSs are modeled with about 150,000 SPH particles per star.

2.2 Merger remnants

In this study we exclusively consider BH-torus systems as possible merger remnants, i.e. we do not explore the case of hyper-/supermassive NSs resulting from binary NS mergers. Since during the remnant evolution neutrino-transport effects in the accretion torus become non-negligible, we use

a different simulation code for the remnants than for the actual mergers (see Sect. 2.1), namely a recently developed finite-volume neutrino-hydrodynamics code described in Obergaulinger (2008) and Just et al. (in preparation).

The BH-torus simulations are performed in axisymmetry and employing Newtonian hydrodynamics. We ignore the self-gravity of the torus, whose mass is much smaller than the BH mass, and for the gravitational potential of the BH we use the pseudo-Newtonian Artemova-potential (Artemova et al. 1996, as given by their Eq. 13).

The Artemova-potential is an extension of the widely employed Paczyński-Wiita-potential (Paczyński & Wiita 1980) that additionally takes into account essential effects of BH rotation. Specifically, compared to the Kerr metric (Bardeen et al. 1972) the potential by Artemova et al. (1996) accurately reproduces the radius of the innermost stable circular orbit (ISCO) as function of the BH mass, M_{BH} , and BH spin parameter, A_{BH} , and it approximately (up to a few per cent) reproduces the gravitational plus kinetic specific binding energy of a test particle orbiting the central BH at the ISCO. These features make the Artemova-potential the preferred choice compared to the Paczyński-Wiita-potential since post-merger BHs are in general fast rotators and therefore the reduced ISCO radius and enhanced (absolute) binding energy can have a sizable impact on the disk evolution and outflow generation. However, the gas kinematics are still treated nonrelativistically and improvements are desirable (see, e.g., Tejeda & Rosswog 2013). Therefore, although we consider the qualitative features of BH rotation that are most relevant to our study to be captured by the Artemova-potential, the quantitative accuracy of our treatment is of course limited and has to be compared against future general relativistic studies.

The BH mass and spin are kept fix during the simulations. Given that the considered torus masses are only a fraction $\xi \leq 0.1$ of the BH masses (see Sec. 3.1), we expect no qualitative and only a small quantitative impact of this approximation on our main results. Note that the maximum possible change ΔA_{BH} of the BH spin parameter due to disk accretion can be estimated by assuming that the entire torus is instantly (i.e. for a fixed BH spin) accreted from the ISCO as $\Delta A_{\text{BH}} \lesssim \xi[\tilde{l} - A_{\text{BH}}(2 + \xi)]/(1 + \xi)^2 < \xi$, where \tilde{l} is the dimensionless Keplerian specific angular momentum at the ISCO (in units of GM_{BH}/c , where G and c are the gravitational constant and the speed of light, respectively) and the last inequality holds for the case $A_{\text{BH}} = 0.8$ (with $\tilde{l} \approx 2.4$) which is exclusively considered in this paper.

For the EOS we assume the fluid to be composed of an ideal Fermi gas of electrons and positrons, of a thermal photon gas, and of a 4-species Boltzmann gas of neutrons, protons, α -particles and a representative, heavy nucleus in the form of ^{54}Mn (whose particular choice does not have any significant relevance for our simulations). The baryonic species are taken to be in nuclear statistical equilibrium (NSE).

The neutrino transport is described by a truncated two-moment scheme, which solves the evolution equations of the energy density and flux density of neutrinos augmented with a closure relation that expresses the Eddington tensor as a function of the evolved quantities. For a detailed description of the formalism and its implementation we refer to a dedicated paper (Just et al., in preparation) and for other implementations of similar schemes the reader may consult, e.g.,

Audit et al. (2002); Shibata et al. (2011); O’Connor & Ott (2013); Skinner & Ostriker (2013); Sądowski et al. (2013). A test problem in which the radiation field of a representative torus configuration is compared against ray-tracing results, together with a brief discussion on the accuracy of our transport treatment can be found in Appendix A. We employ the closure prescription by Minerbo (1978) for the calculations in this study. The transport implementation basically includes all velocity-dependent terms up to $\mathcal{O}(v/c)$. However, since the rotational velocities close to the BH as well as the polar velocities in the axial funnel can reach values comparable to the speed of light but incompatible with our $\mathcal{O}(v/c)$ transport treatment, we limit velocities in the transport equations to $0.2c$. We also omit terms depending on the azimuthal velocity component v^ϕ , thus ignoring the azimuthal components of the neutrino propagation and advection as well as $r\phi$ and $\theta\phi$ components of the neutrino viscosity. This procedure may appear too radical to cope with high rotation velocities occurring just in the close vicinity of the BH and would numerically not be necessary in the whole torus, but it still seems reasonably compatible with our modeling constraint to axisymmetry. Because the torus is axisymmetric the time evolution of the neutrino radiation quantities is mainly driven by radial and lateral transport while the rotational aberration is a secondary effect, at least for rotational velocities not too close to the speed of light.

In our energy-dependent transport scheme we evolve the radiation quantities in discrete energy groups for each species, electron neutrinos and electron antineutrinos. We ignore the effects of heavy-lepton neutrinos, which are of minor relevance during the torus evolution (e.g. Janka et al. 1999; Ruffert & Janka 1999; Deaton et al. 2013; Fernández & Metzger 2013; Foucart et al. 2014). For the neutrino interaction channels we take into account the β -processes with free nucleons and scattering of neutrinos off free nucleons (as formulated in Bruenn 1985), as well as annihilation of neutrino-antineutrino pairs (based on Dicus 1972; Schinder et al. 1987; Cooperstein et al. 1987). Since at later stages of the torus evolution neutrino absorptions become negligible, we switch from the full neutrino-transport scheme to a computationally cheaper treatment assuming neutrinos to be only emitted but not reabsorbed or scattered by the medium. We typically switch to this simplification at some time $t_{\text{switch}} \geq t_\eta$, where t_η is the time when the neutrino emission efficiency η_ν (see Sect. 3.3 for the definition) drops below 0.005. We have validated by tests that t_{switch} is chosen sufficiently late to ensure that effects due to non-vanishing optical-depths are negligible. Depending on the model, the values of t_{switch} lie typically between 0.3 s and 1.5 s.

The initial disk models are constructed as rotational equilibrium configurations with constant specific angular momentum (see, e.g., Iğumenshchev et al. 1996; Stone et al. 1999; Fernández & Metzger 2013, where similar disk models have been used as initial models). For given BH properties M_{BH} and A_{BH} and given torus mass M_{torus} , the fluid configuration is defined by setting the initial electron fraction to $Y_{e,0} = 0.1$ everywhere in the disk (roughly guided by post-merging results), by imposing a polytropic relation $P_0 \propto \rho_0^{4/3}$ to hold between the initial density ρ_0 and pressure P_0 , by fixing the maximum density of the torus to $\rho_{\text{max}} \approx 2.2 \times 10^{12} \times (M_{\text{torus}}/M_\odot) \text{ g cm}^{-3}$, and by placing the inner torus edge to a radius of $r_{\text{min}} = 3r_s$, where r_s

is the Schwarzschild radius corresponding to the chosen BH mass M_{BH} .

We employ the α -viscosity approach by Shakura & Sunyaev (1973) to include the effects of turbulent angular momentum transport in an approximate, parametrized fashion. Since a number of different formulations for the (shear) viscosity tensor $T_{ij} \equiv \eta_{\text{vis}}(\nabla_i v_j + \nabla_j v_i - (2/3)\delta_{ij}\nabla_k v^k)$ and the dynamic viscosity coefficient η_{vis} exist in the literature (with v_i being the velocity components), we exploratively consider two different formulations to test the dependence of our nucleosynthesis results on the explicit choice of the viscosity prescription: In the “type 1” case, which is used for most BH-torus models, we include all components of T_{ij} and the dynamic viscosity coefficient is defined as

$$\eta_{\text{vis,type1}} \equiv \alpha_{\text{vis}} \rho c_s^2 \Omega_{\text{K}}^{-1}, \quad (1)$$

where $c_s \equiv \sqrt{\gamma P/\rho}$ with the adiabatic index γ and Ω_{K} is the Keplerian angular velocity. This prescription was employed, for instance, by Igumenshchev et al. (1996); Lee et al. (2005); Setiawan et al. (2006). In the “type 2” case, in contrast, only the components $T_{r\phi}$ and $T_{\theta\phi}$ are included (i.e. the remaining components are set to 0) and the dynamic viscosity coefficient $\eta_{\text{vis,type2}}$ is computed like $\eta_{\text{vis,type1}}$, cf. Eq. (1), but with the adiabatic sound speed c_s replaced by the isothermal sound speed $c_i \equiv \sqrt{P/\rho}$. This prescription was used, for instance, by Fernández & Metzger (2013). Note that for the type 2 viscosity, in contrast to the type 1 case, shear motions in meridional planes remain unaffected by viscosity. As a consequence, the development of small-scale vorticity is less suppressed and the fluid pattern appears less laminar than for the viscosity treatment of type 1. Furthermore, for a given value of α_{vis} the dynamic viscosity coefficients (which are a measure of the “strength” of viscosity) for both prescriptions are related by

$$\eta_{\text{vis,type2}} = \frac{1}{\gamma} \eta_{\text{vis,type1}} \approx (0.6 \dots 0.8) \times \eta_{\text{vis,type1}}. \quad (2)$$

For all BH-torus simulations we take 416×160 grid cells to cover the domain $(r, \theta) \in [10 \text{ km}, 2.5 \times 10^4 \text{ km}] \times [0, \pi]$. We use non-uniform grids in both coordinate directions with the radial cell size increasing roughly proportionally to the radius and the angular grid ensuring a resolution around the equatorial plane slightly better than at the poles. We employ 10 logarithmically spaced energy groups spanning the range of 0 – 80 MeV to cover the neutrino-energy space. For numerical reasons we need to define a (local) minimum gas density value to which the evolved density is reset whenever it drops below this value. We choose this floor density, ρ_{floor} , to have a radially decreasing and time-dependent profile: Initially, ρ_{floor} monotonically decreases with $\rho_{\text{floor}} \simeq 10^5, 10^2, 10^{-3} \text{ g cm}^{-3}$ at radii $r = 10, 10^3, 2.5 \times 10^4 \text{ km}$, respectively. During the first ~ 200 ms of evolution we continuously decrement the floor density in the region $r \in [10 \text{ km}, 1000 \text{ km}]$ down to a final, constant value of 10^2 g cm^{-3} . At the start of each simulation, we fill the volume surrounding the torus with an ambient medium that has 1.5 times the floor density, resulting in a total mass of $\sim 4 \times 10^{-6} M_{\odot}$ for the initial ambient medium.

2.3 Nucleosynthesis

The r-process nucleosynthesis is calculated by post-processing a representative set of trajectories for the ejected matter, taking into account the dynamics as determined by the hydrodynamics simulation. The number of post-processed trajectories per model typically lies between a few hundred for the merger models and a few thousand for the BH-torus models. The temperature evolution is estimated on the basis of the laws of thermodynamics, allowing for possible nuclear heating through beta-decays, fission, and alpha-decays, as described in Meyer (1989). Also, for the late-time evolution the ejecta dynamics includes the pressure feedback by nuclear heating through the approximative model described in Goriely et al. (2011a). The nucleosynthesis is followed with a reaction network including all 5000 species from protons up to $Z=110$ that lie between the valley of β -stability and the neutron-drip line. All charged-particle fusion reactions on light and medium-mass elements that play a role when the NSE freezes out are included in addition to radiative neutron captures and photodisintegrations. The reaction rates on light species are taken from the NETGEN library, which includes all the latest compilations of experimentally determined reaction rates (Xu et al. 2013). Experimentally unknown reactions are estimated with the TALYS code (Koning et al. 2005; Goriely et al. 2008) on the basis of the Skyrme Hartree-Fock-Bogolyubov (HFB) nuclear mass model, HFB-21 (Goriely et al. 2010). On top of these reactions, β -decays as well as β -delayed neutron emission probabilities are also included, the corresponding rates being taken from the updated version of the Gross Theory (Tachibana et al. 1990) based on the same HFB-21 Q -values.

All fission rates, i.e. the neutron-induced, photo-induced, β -delayed and spontaneous fission rates, are estimated on the basis of the HFB-14 fission paths (Goriely et al. 2007) and the nuclear level densities within the combinatorial approach (Goriely et al. 2008) obtained with the same single-particle scheme and pairing strength. The neutron- and photo-induced fission rates are estimated on the basis of the TALYS code for all nuclei with $90 \leq Z \leq 110$ (Goriely et al. 2009). Similarly, the β -delayed and spontaneous fission rates are estimated with the same TALYS fission barrier penetration calculation. The β -delayed fission rate takes into account the full competition between the fission, neutron and photon channels, weighted by the population probability given by the β -decay strength function (Kodama & Takahashi 1975). The fission fragment yield distribution is estimated with the renewed statistical scission-point model based on microscopic ingredients, the so-called SPY model, and described in Panebianco et al. (2012); Goriely et al. (2013).

3 RESULTS

3.1 Choice of global parameters and coherence of modeling approach

In Table 1 we summarize the investigated merger models and their properties. The employed microphysical EOSs are SFHO (Steiner et al. 2013), SFHX (Steiner et al. 2013), TM1 (Sugahara & Toki 1994; Hempel et al. 2012), TMA (Toki et al. 1995; Hempel et al. 2012), and DD2

Table 1. Parameters and outflow properties for the merger models. The columns contain from left to right: Model name, masses of the binary components (with M_2 being the initial BH mass in the NS-BH cases), spin parameter of the initial BH (only NS-BH; in all cases prograde with the orbital motion), equation of state, prompt (pc) or delayed (dc) collapse (only NS-NS), mass and spin parameter of the BH remnant, mass of the remnant torus, mass of the dynamical ejecta, asymmetry parameter (see Sect. 3.2 for the definition), mean electron fraction \bar{Y}_e , mean entropy \bar{s} and mean outflow velocity \bar{v} of the dynamical ejecta, and the name of the corresponding BH-torus model. The quantities \bar{Y}_e , \bar{s} and \bar{v} are measured 5 ms after the merger.

Merger model	M_1 [M_\odot]	M_2 [M_\odot]	$A_{\text{BH},0}$	EOS	pc/dc	M_{BH} [M_\odot]	A_{BH}	M_{torus} [M_\odot]	M_{dyn} [$10^{-3} M_\odot$]	B_{asy}	\bar{Y}_e	\bar{s}/k_{B}	\bar{v} [10^{10} cm/s]	Remnant model
SFHO_1218	1.2	1.8		SFHO	pc	2.78	0.76	0.137	4.9	0.28	0.036	9.9	1.19	M3A8m1...
SFHO_13518	1.35	1.8		SFHO	pc	2.97	0.78	0.099	4.3	0.16	0.036	6.7	1.28	M3A8m1...
SFHX_1515	1.5	1.5		SFHX	dc	2.77	0.78	0.106	21.2	0.01	0.032	8.2	0.67	M3A8m1...
SFHO_145145	1.45	1.45		SFHO	dc	2.68	0.79	0.091	14.3	0.02	0.033	7.9	0.64	M3A8m1...
TM1_175175	1.75	1.75		TM1	pc	3.37	0.85	0.027	8.4	0.07	0.027	10.0	1.12	M3A8m03...
TMA_1616	1.6	1.6		TMA	dc	3.04	0.83	0.037	5.2	0.07	0.012	5.4	0.62	M3A8m03...
TM1_1123	1.1	2.29	0.54	TM1		3.04	0.81	0.30	79.8	0.93	0.056	0.64	0.66	M3A8m3...
SFHO_1123	1.1	2.3	0.53	SFHO		3.09	0.82	0.26	40.4	0.96	0.042	0.73	0.60	M3A8m3...
DD2_14529	1.45	2.91	0.53	DD2		4.00	0.83	0.27	35.9	0.96	0.056	0.62	0.67	M4A8m3...
TM1_1430	1.4	3.0	0.52	TM1		4.03	0.81	0.30	45.8	0.97	0.054	0.50	0.67	M4A8m3...
TM1_14051	1.4	5.08	0.70	TM1		6.08	0.83	0.32	55.8	0.98	0.050	0.41	0.75	M6A8m3...

Table 2. Parameters and outflow properties for the relic BH-torus models. The columns from left to right contain: Model name, mass and spin parameter of the BH, torus mass, value of viscosity parameter, settings for viscosity type, radioactive heating and neutrino heating, total outflow mass, neutrino-driven outflow mass, and the mean electron fraction \bar{Y}_e , mean entropy \bar{s} and mean velocity \bar{v} of the outflow. The two quantities \bar{Y}_e and \bar{s} are measured when the outflow temperatures drop below 5 GK, and \bar{v} is evaluated at a fixed radius of $r = 10^4$ km.

Remnant model	M_{BH} [M_\odot]	A_{BH}	M_{torus} [M_\odot]	α_{vis}	visc. type	radio. corr.	neutr. heat.	M_{out} [$10^{-3} M_\odot (M_{\text{torus}})$]	$M_{\text{out},\nu}$ [$10^{-3} M_\odot (M_{\text{torus}})$]	\bar{Y}_e	\bar{s}/k_{B}	\bar{v} [10^9 cm/s]
M3A8m3a2	3	0.8	0.3	0.02	type 1	No	Yes	66.8 (22.3%)	3.00 (1.00%)	0.28	20.9	1.16
M3A8m3a5	3	0.8	0.3	0.05	type 1	No	Yes	78.3 (26.1%)	3.51 (1.17%)	0.25	23.0	1.55
M3A8m1a2	3	0.8	0.1	0.02	type 1	No	Yes	22.7 (22.7%)	0.09 (0.09%)	0.28	24.8	1.03
M3A8m1a5	3	0.8	0.1	0.05	type 1	No	Yes	24.7 (24.7%)	0.35 (0.35%)	0.24	28.0	1.56
M3A8m03a2	3	0.8	0.03	0.02	type 1	No	Yes	7.0 (23.4%)	0.0005 (0.002%)	0.27	29.5	0.96
M3A8m03a5	3	0.8	0.03	0.05	type 1	No	Yes	7.3 (24.3%)	0.002 (0.007%)	0.25	32.7	1.70
M4A8m3a5	4	0.8	0.3	0.05	type 1	No	Yes	66.2 (22.1%)	1.47 (0.49%)	0.26	28.1	1.66
M6A8m3a5	6	0.8	0.3	0.05	type 1	No	Yes	56.3 (18.8%)	0.07 (0.02%)	0.27	29.4	1.45
M3A8m3a2-v2	3	0.8	0.3	0.02	type 2	No	Yes	64.2 (21.4%)	2.58 (0.86%)	0.29	19.3	0.97
M3A8m3a5-v2	3	0.8	0.3	0.05	type 2	No	Yes	70.1 (23.4%)	2.63 (0.88%)	0.26	19.7	1.39
M4A8m3a5-rh	4	0.8	0.3	0.05	type 1	Yes	Yes	67.3 (22.4%)	1.51 (0.50%)	0.26	26.4	1.62
M3A8m1a2-rh	3	0.8	0.1	0.02	type 1	Yes	Yes	22.8 (22.8%)	0.09 (0.09%)	0.28	25.1	1.05
M3A8m3a2-noh	3	0.8	0.3	0.02	type 1	No	No	56.6 (18.7%)	–	0.24	21.7	0.90

(Typel et al. 2010; Hempel & Schaffner-Bielich 2010), which are all derived within the relativistic mean-field approach. These EOSs are compatible with the current limit on the maximum NS mass of about $2 M_\odot$ (Demorest et al. 2010; Antoniadis et al. 2013). For the NS-NS mergers we consider three models which result in the direct formation of a BH immediately after merging (within $\lesssim 1-2$ ms, “prompt collapse”). In addition, we simulate three setups which lead to a “delayed collapse” after sufficient angular momentum has been redistributed and radiated away by gravitational waves. The lifetimes of the relic NSs in these cases are roughly 10 ms. In our study we do not consider cases where a metastable, long-lived ($\gtrsim 20$ ms) or even stable massive NS is formed. We therefore do not investigate here the potentially relevant outflow component which may arise during the lifetime of such a massive NS (Dessart et al. 2009; Metzger & Fernández 2014; Perego et al. 2014). For the NS-BH merger models we examine cases in which relic BHs with masses $M_{\text{BH}} \simeq 3, 4$ and $6 M_\odot$ are formed, varying the EOS between TM1, SFHO and DD2. In all simulated cases the

initial BH spin (with dimensionless spin parameter $A_{\text{BH},0}$ between 0.5 and 0.7) is assumed to be prograde with the orbital motion.

The merger models chosen here are not the most typical cases concerning what is expected from observations of NS-NS binaries (e.g. Lattimer 2012) and binary population models of NS-NS and NS-BH systems (e.g. Dominik et al. 2012). For the NS-NS case the most likely configuration with $M_1 \simeq M_2 \simeq 1.4 M_\odot$ leads to a long-lived massive NS for most choices of the EOS (Bauswein et al. 2013b). Instead, we focus here on NS-NS models which collapse within the simulation time and produce remnant configurations that match the initial conditions for our long-term evolution studies of BH-torus systems. Note, however, that the relic BH-torus models considered in our work may also represent remnants formed in cases where the NS collapses to a BH with some longer delay.

The transition from the merger models to the relic BH-torus models is realized in an approximate manner by setting up BH-torus models in rotational equilibrium as described

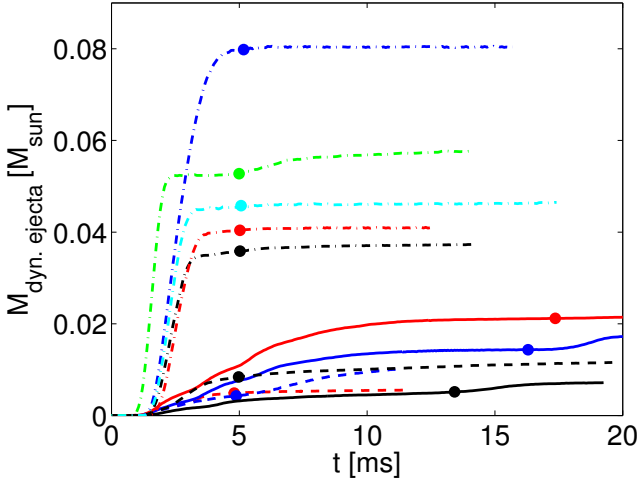


Figure 2. Prompt (“dynamical”) mass ejection in our NS-NS and NS-BH merger simulations as function of time. The curves show the cumulative mass beyond a radius of 150 km that fulfills the criterion to be gravitationally unbound (see Bauswein et al. 2013b). The solid lines correspond to NS-NS cases with delayed collapse of the merger remnant to a BH (red: SFHX_1515, blue: SFHO_145145, black: TMA_1616), the dashed lines to NS-NS cases with prompt BH formation (red: SFHO_1218, blue: SFHO_13518, black: TM1_175175), and the dash-dotted lines belong to the NS-BH mergers (blue: TM1_1123, green: TM1_14051, cyan: TM1_1430, red: SFHO_1123, black: DD2_14529). The bullets indicate the times when the ejecta masses for the merger phase are determined, assuming that the subsequent remnant evolution is covered by our BH-torus simulations.

in Sect. 2.2, specifying values for the BH mass M_{BH} , BH spin A_{BH} and torus mass M_{torus} motivated by and approximately equal to the corresponding values in the merger models. Therefore, each merger model can be associated with one or several BH-torus models (see Table 1). Given the limited compatibility of the codes used for simulating the merger and merger remnant evolutions, this is a pragmatic approach which should be replaced by a fully consistent treatment of both evolutionary phases in future models. However, our approach of examining both phases separately is advantageous insofar as different progenitors may lead to very similar BH-torus systems and therefore the BH-torus models are representative of a larger variety of binary merger configurations than investigated in the present study.

In Table 2 the properties of the investigated BH-torus models are summarized. Given the selection of merger models, the set of BH-torus models allows us to explore the dependence of the nucleosynthesis production on variations of the torus mass, the BH mass, and the viscosity parameter α_{vis} . The two additional models with suffix ‘v2’ are set up to study the impact of the specific choice for the viscosity prescription (cf. Sect. 2.2). Moreover, since the heating feedback due to radioactive decays of newly formed r-process nuclei is not consistently included in our standard hydrodynamical simulations (but only in the post-processing calculations for the nucleosynthesis), we examine two more models (with suffix ‘rh’), in which radioactive heating is approximated in the following way: First, the radioactive heating rates, $Q(t_{\text{nuc}})$, and temperatures, $T(t_{\text{nuc}})$, for all outflow trajectories of the standard models are averaged (where t_{nuc} is the

time during nucleosynthesis, normalized such that $t_{\text{nuc}} = 0$ at $T = 10$ GK). Then the resulting average heating rate, $\langle Q \rangle(t_{\text{nuc}})$, is interpreted as a function of the average temperature, $\langle Q \rangle(T) \equiv \langle Q \rangle(t(\langle T \rangle))$, and applied in the ‘rh’-simulations as additional energy source term in the energy equation for all cells with $T \leq 10$ GK and positive radial velocities. We also examine the effects of neutrino heating by considering model M3A8m3a2-noh, which is set up in analogy to model M3A8m3a2 but with all neutrino source terms in the gas-energy and momentum equations being switched off in regions where net heating by neutrinos applies, i.e., where energy is transferred from neutrinos to the stellar medium.

3.2 Compact binary mergers

For any type of compact-object binary the merging occurs after an inspiral phase, in which the gravitational-wave emission and the corresponding angular momentum loss lead to a shrinking of the orbital separation. The secular inspiral of the binary components proceeds increasingly faster until the system enters the dynamical merging phase. The ejecta masses (Fig. 2) as well as the exact conditions in the ejecta and the properties of the remaining tori depend on the dynamics of the compact object mergers. We briefly describe the dynamics of three typical models which represent different formation channels for relic BH-torus systems and for which the merging process possibly leaves an imprint on the properties of the ejecta. All simulated binary mergers belong to one of these three categories of events.

Delayed collapse (TMA_1616). The coalescence of two NSs of $1.6 M_{\odot}$ with the TMA EOS leads to the formation of a single, massive, differentially rotating NS, which is supported against gravitational collapse by centrifugal forces and thermal pressure. The remnant consists of a rotating double-core structure with the two dense cores bouncing against each other. The associated redistribution of angular momentum and the emission of gravitational waves generated by the oscillations of the merger remnant cause the collapse of the central object to a BH about 9 ms after merging. Matter with high angular momentum forms a torus of about $0.037 M_{\odot}$ surrounding the central BH, which has a spin parameter of ~ 0.83 .

During the final collision of two NSs, matter is scraped off from the NS surfaces and squeezed out from their joint contact interface to become unbound in waves created by violent pulsations of the rapidly rotating, massive NS remnant. Most of the dynamical ejecta are produced within less than 10 ms after the merging (Fig. 2). The ejecta mass still increases at later times and even after the BH formation. However, we do not take into account such late ejecta produced in our merger models because of their low resolution after the BH formation and because this evolutionary phase is intended to be partially covered by our BH-torus models, where neutrino effects are included, in contrast to the merger simulations. In this work we conservatively determine the dynamical ejecta (cf. Table 1 and Fig. 2) by requiring that matter has moved at least 150 km away from the merger site in addition to applying the formal ejecta criterion of positive total specific energy. This condition ensures that the matter truly becomes unbound, but it may slightly underestimate the total ejecta mass by about 10 per

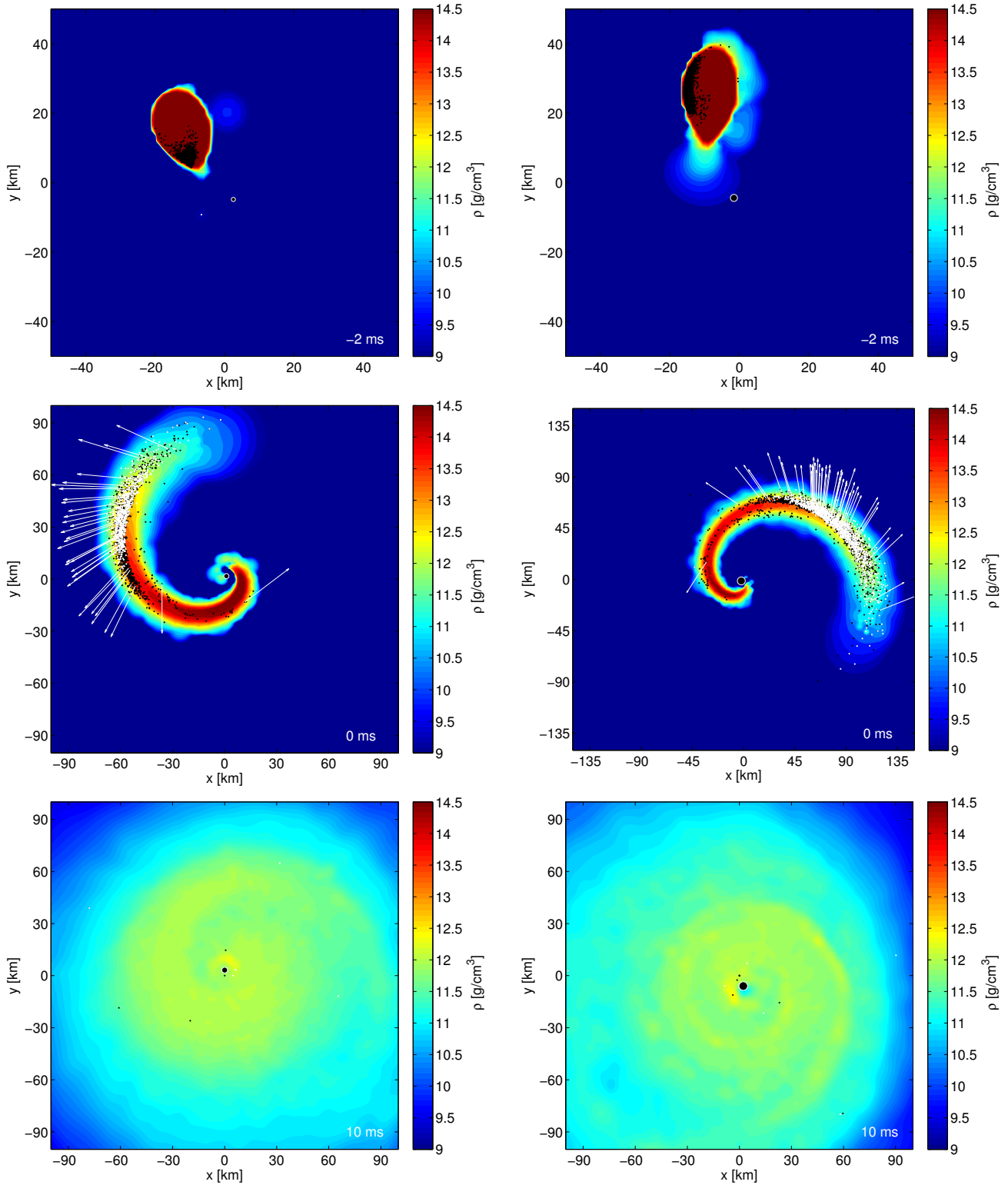


Figure 3. Evolution of the rest-mass density in the equatorial plane for two NS-BH merger models. The left panels correspond to model DD2_14529, which describes the merging of a $1.45 M_{\odot}$ NS and a $2.9 M_{\odot}$ BH with a spin parameter of 0.53 for the DD2 EOS, the right panels display model TM1_14051, which is the coalescence of a $1.4 M_{\odot}$ NS and a $5.1 M_{\odot}$ BH with a spin parameter of 0.7 for the TM1 EOS. The time is given in the lower right corner and is normalized to the moment when the BH has accreted half of the NS matter. The position of the BH is indicated by a filled black circle, whose radius in isotropic coordinates is defined by the gravitational mass of an isolated, nonrotating BH. The dots trace SPH particles (projected into the equatorial plane) which eventually become unbound during the simulations. White dots denote particles which fulfill the ejecta criterion at the current time, while black dots indicate particles that will only become unbound later on. For a subset of SPH particles the arrows visualize the coordinate velocities of the corresponding fluid elements with the length of the arrows being proportional to the velocity. An arrow length of 10 km corresponds to 0.2 times the speed of light. The visualization tool SPLASH was used to convert SPH data to grid data (Price 2007).

cent. As documented in Table 1, the ejecta are very neutron rich, because they originate from the inner crust of the original NSs. The outflow has an average velocity of about $0.6 \times 10^{10} \text{ cm s}^{-1}$ and is fairly isotropic with a moderate preference towards the orbital plane and corresponding suppression in the polar regions (see, e.g., Bauswein et al. 2013b). A detailed description of the formation and dynamics of such ejecta from NS mergers with delayed BH formation was provided by Bauswein et al. (2013b). Recently, Wanajo et al. (2014) pointed out a possible importance of neutrino emission and absorption for reducing the neutron excess in the escaping material. We will discuss this aspect in Sect. 3.4.1.

We note in passing that the stability or instability of the NS-NS merger remnant, the timescale until it collapses to a BH, and the ejecta (and torus) masses depend sensitively on the total binary mass and the NS EOS. Less massive systems and/or stiff nuclear EOSs tend to yield remnants that do not collapse within typical simulation times of ~ 20 ms after the merging. More compact NSs (corresponding to softer nuclear EOSs) lead to higher ejecta masses, more massive binaries produce more dynamical ejecta for a given EOS, and unequal-mass binary mergers also result in more unbound matter than mergers of symmetric systems (Bauswein et al. 2013b). The TMA EOS is relatively stiff in the sense that its NS radii are large. The ejecta and torus masses are therefore small. In contrast, the SFHX and SFHO EOS are on the softer side with smaller NS radii and correspondingly larger ejecta and torus masses.

Prompt collapse (SFHO.13518). For the SFHO EOS the merging of a $1.35 M_{\odot}$ NS and a $1.8 M_{\odot}$ NS results in a direct collapse, i.e., in BH formation only about one millisecond after the stars touch. The less massive NS is tidally strongly stretched before and during the merging and forms a massive tidal tail. This tidal tail winds around the BH, collides with itself after one orbit, and most of it ends up in a torus. The torus comprises a mass of about $0.1 M_{\odot}$, and the BH obtains angular momentum which corresponds to a spin parameter of roughly 0.8.

Prompt mass ejection happens during a short period of less than 5 ms (Fig. 2). A substantial fraction of several ten per cent of these ejecta originate from the collision interface, from where they are squeezed out and pushed away by the expanding torus. The rest of the ejecta is originally located in the tidal tail and becomes unbound by tidal forces. The mass loss can slowly continue even later than 10 ms after the merging due to angular momentum transfer within the torus, but for better comparison with the other models we do not include these late ejecta obtained in the merger simulations, because we consider the remnant evolution to be followed by our BH-torus models.

Also in the prompt collapse scenario the spatial distribution of unbound material is nearly isotropic with somewhat less matter being expelled towards the poles than close to the orbital plane (in the two polar cones with half-opening angle of 45° the ejecta mass is roughly a factor of two smaller than in the other directions). Again the ejecta originate from very neutron-rich layers of the initial NSs, which implies an average electron fraction of 0.04. Typical expansion velocities of about 0.4 times the speed of light are somewhat higher than in the models resulting in a delayed collapse, which have average outflow velocities of ~ 20 per cent of the speed of light. The other merger models with prompt

collapse show outflow properties similar to those of model SFHO_13518.

Prompt BH formation is unlikely to be the generic outcome of NS mergers, because NS binary observations (see compilation in Lattimer 2012) and theoretical population synthesis studies of binaries (e.g., Dominik et al. 2012) suggest that most binary systems possess a total mass of about $2.7 M_{\odot}$. For such systems a prompt BH-collapse of the merger remnant is not expected for any EOS that is compatible with the current observational lower limit of the maximum NS mass (cf. Bauswein et al. 2013a for a determination of the threshold mass for direct BH formation in dependence of the binary parameters and EOS).

NS-BH merger (DD2_14529). Figure 3 (left panels) exemplifies the merging of a NS-BH binary with a mass ratio of two and an initial BH spin parameter of roughly 0.5. For the same model, we show in Fig. 4 the properties of the dynamical ejecta in terms of mass distribution histograms for the electron fraction, entropy per baryon, expansion timescale and outflow velocity. During the late inspiral phase the NS is tidally deformed and develops a cusp pointing towards the BH. As the star approaches the BH, mass transfer sets in from this cusp and the NS is stretched into an extended, spiral-arm-like tidal tail. While mass is shed off the far end of the tidal arm to expand outwards, the matter at the near end wraps the BH and, if it has sufficiently high angular momentum, performs a full orbit around the BH to collide with the spiral arm. Finally, the matter remaining outside the BH assembles into a nearly axisymmetric torus of about $0.27 M_{\odot}$. Accretion from this torus continues at a lower rate and the configuration reaches a quasi-steady state. At this time the BH mass has grown to $4 M_{\odot}$ and the BH spin parameter has increased to approximately 0.8.

When about half of the NS mass has been accreted, matter located at the outer edge of the spiral arm becomes gravitationally unbound by tidal effects within about one millisecond (visualized in Fig. 3, middle panels for $t = 0$). A smaller fraction (approximately 10 per cent of the total ejecta mass) is expelled during the subsequent evolution, in particular when the tip of the spiral arm collides with the main body of the arm. The unbound matter originates mostly from the inner crust of the NS and therefore is very neutron-rich (Y_e ranges between 0.02 and 0.08, see Fig. 4, left panel). The dominant ejection of decompressed, unshocked matter from the tidally disrupted NS is reflected by the pronounced peak at entropies below $1 k_B$ per nucleon¹ in the second panel of Fig. 4. Typical ejecta velocities (at 10 ms after the NS-BH merging) are 15–25% of the speed of light (right panel of Fig. 4), similar to those obtained for the delayed collapse cases of NS-NS mergers.

As a consequence of the ejection mechanism, the outflow is highly asymmetric. To quantify the asymmetry we identify the hemisphere where the main ejecta mass, M_+ , is produced and the opposite hemisphere (ejecta mass M_-) and define the asymmetry parameter B_{asy} by $B_{\text{asy}} \equiv (M_+ -$

¹ Note that in Table 1 we report entropies obtained from a post-processing procedure that reduces the effects caused by heating due to numerical viscosity in the SPH code. These entropies are also applied for our nucleosynthesis calculations (see Goriely et al. 2011b).

$M_-)/(M_+ + M_-)$ with $(M_+ + M_-)$ being the total ejecta mass. Symmetric mass ejection corresponds to $B_{\text{asy}} \sim 0$, highly asymmetric to $B_{\text{asy}} \sim 1$. For model DD2_14529 we determine an asymmetry of 0.96 and observe similar values for the other NS-BH merger cases investigated in our study. These findings are in line with the anisotropy reported in Kyutoku et al. (2013). In contrast, NS mergers show much smaller asymmetries of the order of only a few per cent for symmetric and nearly symmetric systems and some 10% for highly asymmetric binaries (see Table 1).

The right panels of Fig. 3 display the merging of a NS with a more massive BH of about $5 M_\odot$ and a spin parameter of 0.7 (model TM1_14051), which according to population synthesis studies (Dominik et al. 2012) may represent an astrophysically more typical case. The merger dynamics and ejecta production proceeds qualitatively similarly to the case of model DD2_14529. Comparing the rest-mass density in the equatorial plane the more massive model evolves in close analogy to the simulation with a mass ratio of 3 in (Kyutoku et al. 2011, see their Fig. 2). Note that we employ a stiff EOS (TM1), which tends to compensate for the somewhat lower mass ratio and slightly higher spin used in Kyutoku et al. (2011). Quantitatively, our model compares well with the calculation 2H-Q3M135a75 of this paper (stiff EOS, mass ratio 3, initial BH spin parameter 0.75), which results in a torus of $0.35 M_\odot$ and a final value of the spin parameter of 0.86. Our model TM1_14051 is also compatible with the $Q = 3$ simulation with the MS1 EOS and a BH spin parameter of 0.75 in Kyutoku et al. (2013). The authors of the latter work report an ejecta mass of $0.07 M_\odot$, which is in satisfactory agreement with $0.055 M_\odot$ of unbound matter found in our simulation.

3.3 Merger Remnants

In Sect. 3.3.1 we describe basic features of the evolution of BH-tori as NS-NS or NS-BH merger remnants and the corresponding phases and components of mass loss. Sects. 3.3.2 and 3.3.3 will present an overview of the corresponding ejecta masses and properties, respectively. In Sect. 3.3.4 our results will be briefly compared with recent models published by Fernández & Metzger (2013). More details of our BH-torus evolution simulations will be provided in a forthcoming paper by Just, Janka & Obergaulinger (in preparation).

3.3.1 Torus evolution, neutrino emission, and ejecta production

Depending on their initial mass, accretion tori as merger remnants evolve on timescales of milliseconds to seconds by losing mass to the accreting BH and in thermally, magnetically and viscously driven outflows. In our hydrodynamic models the effects of magnetic fields are simplified by the standard treatment through Shakura-Sunyaev α -viscosity terms (Shakura & Sunyaev 1973). For the high densities (10^9 g cm^{-3} and higher) and mass accretion rates ($\sim 10^{-2} M_\odot \text{ s}^{-1}$ to several $M_\odot \text{ s}^{-1}$) characteristic of the post-merger configurations, the tori cool predominantly by neutrino emission while photons are trapped and contribute to the pressure as a plasma component in thermal equilibrium with electrons, positrons, nucleons and nuclei (see, e.g.,

Popham et al. 1999; Kohri & Mineshige 2002; Di Matteo et al. 2002).

Sufficiently massive and initially dense tori are known to evolve through three stages of radiation efficiency and correspondingly different mass-loss properties (cf., for example, Metzger et al. 2008, 2009; Beloborodov 2008; Fernández & Metzger 2013): (1) High initial densities produce optically thick conditions for neutrinos so that neutrinos are trapped and therefore neutrino cooling is inefficient (see, e.g. Di Matteo et al. 2002). (2) As the torus mass decreases and densities drop, the so-called NDAF (Neutrino-Dominated Accretion Flow, Popham et al. 1999) state is reached, in which gravitational energy that is converted to internal energy by viscous heating is essentially completely radiated away by neutrinos. (3) Eventually, when mass, density, and temperature of the torus decrease further, the neutrino production rate becomes so low that neutrino cooling is inefficient again. In this phase of an advection-dominated accretion flow (ADAF, Narayan & Yi 1994) viscous heating leads to large-scale convective motions and powers a strong expansion of the torus (for simulations of viscous ADAFs, see, e.g., Igumenshchev et al. 1996; Igumenshchev & Abramowicz 1999; Stone et al. 1999).

During stages (1) and (2) the high neutrino luminosities emitted by the dense, inner parts of the torus irradiate and heat the outer, more dilute layers of the torus. Doing so they can launch a mass outflow from this neutrino-heated (or “gain”) region, which has similarities to the neutrino-driven wind blown off the surface of new-born, hot neutron stars in supernova cores (e.g., Qian & Woosley 1996). The mass-loss rate as well as the thermodynamic conditions and the neutron-to-proton ratio of these ejecta are sensitive functions of the neutrino emission properties of the torus, but different from nascent neutron stars the BH-torus systems are extremely nonspherical. During the ADAF phase viscous angular momentum transport as well as dissipative heating by shear viscosity lead to an inflation of the torus, driving outward mass flows near the equatorial plane but also launching mass loss away from the equator. In contrast to the neutrino-driven mass ejection, viscously driven expansion proceeds gradually and continuously, and the matter becomes gravitationally unbound only at large radii and with lower velocities than the supersonic neutrino-driven wind.

The first, optically thick period lasts at most ~ 10 – 30 ms for initial torus masses considered in this work. Some smaller contribution to the mass ejection by neutrino heating happens already in this phase. However, since our initial BH-tori are artificially constructed as equilibrium models rather than being direct results from merger simulations, one should apply great caution in interpreting the ejecta of this intermediate stage between the post-merger remnant and the relaxed, neutrino radiating, quasi-steady-state torus. Fortunately, the mass loss during this transition phase is far subdominant in the total ejecta budget. In Fig. 5 we provide representative snapshots for the two following evolutionary phases for model M3A8m3a5, the NDAF phase (top row of plots, 0.05 s after the start of the simulation) and the ADAF phase (bottom row of plots, for $t = 2.0$ s). For this particular model the NDAF phase lasts about 250 ms be-

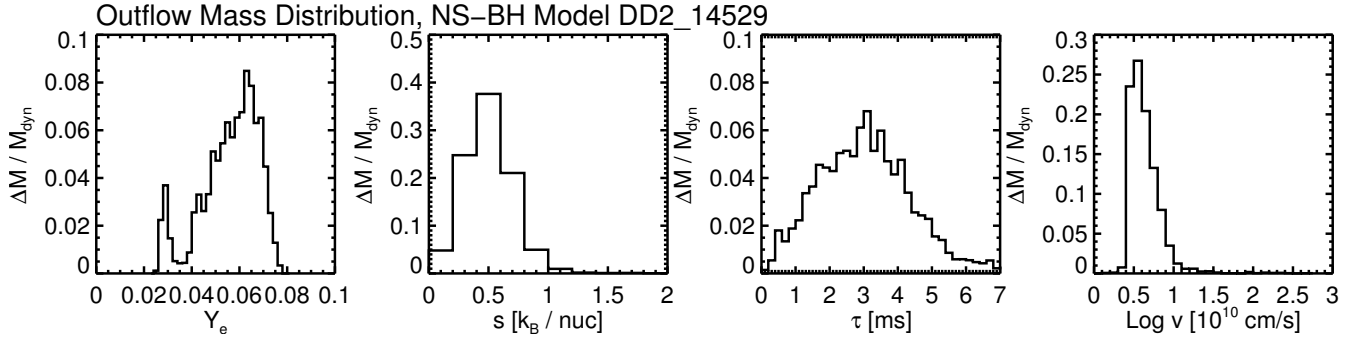


Figure 4. Mass-distribution histograms for the dynamical ejecta of the NS-BH merger model DD2_14529. All distributions are normalized to the total mass of dynamical ejecta, $M_{\text{dyn}} = 3.59 \times 10^{-2} M_{\odot}$. From left to right the panels show the mass distributions for the electron fraction Y_e , entropy per baryon s (both measured about 5 ms after the merging), expansion timescale τ (measured here as the time within which the density decreases from $10^{12} \text{ g cm}^{-3}$ to $10^{10} \text{ g cm}^{-3}$), and outflow velocity v (measured about 10 ms after the merging). The small peak at low Y_e and the adjacent local minimum are artifacts caused by SPH-particle clustering in the initial model of the NS. This distortion of the Y_e mass distribution does not affect the nucleosynthesis results.

fore a steep decrease of the neutrino luminosities² indicates the transition to the ADAF stage (Fig. 6, top panel), but depending on the torus mass and viscosity parameter—the BH mass has less influence—the duration of the NDAF can be between less than ~ 0.1 s and more than ~ 1 s.

Because of the initially very neutron rich conditions ($Y_{e,0} = 0.1$), the torus protonizes (see Fig. 6, where the time evolution of the mean electron fraction of the torus, Y_e^{torus} , is plotted) by radiating more electron antineutrinos, $\bar{\nu}_e$, produced in positron captures on neutrons than electron neutrinos, ν_e , emitted by electron captures on protons. Since the mean energies are ordered in the same hierarchy, $\varepsilon_{\bar{\nu}_e} > \varepsilon_{\nu_e}$, the $\bar{\nu}_e$ luminosity is also higher than the ν_e luminosity in all cases (Fig. 6). These findings are fully compatible with previous simulations of post-merger accretion tori (e.g., Ruffert & Janka 1999; Setiawan et al. 2006; Deaton et al. 2013; Foucart et al. 2014).

Also the neutrino-emission efficiency η_{ν} , defined by

$$L_{\nu_e} + L_{\bar{\nu}_e} = \eta_{\nu} \dot{M}_{\text{acc}} c^2 \quad (3)$$

as the ratio of the total neutrino luminosity to the rate of rest-mass energy accreted by the BH, is a clear indicator of the three evolutionary stages of the accretion tori. During phase (1) the efficiency is lower than in the NDAF phase (2)³ and drops at the transition to the ADAF phase (Fig. 6, third panel). In the NDAF phase the values of η_{ν} are approximately constant and range between a few per cent and nearly 10%, close to the energy-loss efficiency calculated for test masses accreted through the innermost stable circular orbit.

In Fig. 5a, left panel, the black area indicates the dense, inner parts of the torus, where neutrino cooling exceeds

heating. Outside of this region the net heating (i.e., heating minus cooling) rate is color coded. Heating is strongest above the torus and exhibits steep decrease with growing vertical and horizontal distance from the BH, in whose vicinity the plasma temperature is highest. The neutrino-driven wind develops at about 150 km and fills a wide cone with half-opening angle of about 65° around the polar axis (at a radius of 1000 km). Within this cone the outflowing matter has electron fractions Y_e larger than ~ 0.3 and entropies, s , of more than $\sim 10 k_B$ per nucleon (Fig. 5b). The viscously driven outflow during the ADAF phase, which is visible in plots (c) and (d) of Fig. 5, is distinctly different not only by being driven outwards also close to the equator, but also by considerably wider distributions of Y_e (including values as low as 0.1) and entropy (see also Fig. 9 and Sect. 3.3.3).

In our nucleosynthesis study we neglect all expelled material with entropies per baryon in excess of $1000 k_B$. Ejecta with such high entropies are driven by the energy deposition through neutrino-antineutrino pair annihilation in cases and phases where a low-density funnel around the polar axis is formed. This jet-like, baryon-poor outflow can reach Lorentz factors beyond 100 and is considered as possible source of short gamma-ray bursts (e.g. Paczynski 1986; Eichler et al. 1989; Jaroszynski 1993; Ruffert & Janka 1999; Aloy et al. 2005). The physical and numerical limitations of our present simulations (with a nonrelativistic code, which requires to set a lower density limit in the axial funnel) do not allow us to treat these high-entropy outflows accurately. We therefore do not investigate the associated nucleosynthesis. Since the mass of these ejecta is several orders of magnitude lower than that of the dominant merger ejecta, their contribution to the overall abundance yields can safely be ignored.

3.3.2 Ejecta masses

Figure 7 shows the time evolution of the mass-outflow rates (integrated over all directions; bottom panel) for four representative torus models and the corresponding average properties of the ejecta (mean electron fraction, entropy, and velocity, from the top to the third panel), measured at a distance of 10^4 km from the BH. The approximate transition times t_{ν} between the NDAF state with its strong neutrino-

² We stress that the term “luminosity” is used here for denoting the total energy loss rate of the torus. Of course, because of the pronounced direction dependence of the neutrino flux with a clear preference for small angles around the polar axis (cf. Fig. 5a, left panel) this quantity is not measurable for observers in any direction.

³ The initial overshooting of η_{ν} is a consequence of the rotational equilibrium setup for the initial torus models, which causes some time delay until the mass accretion rate increases in response to viscous effects.

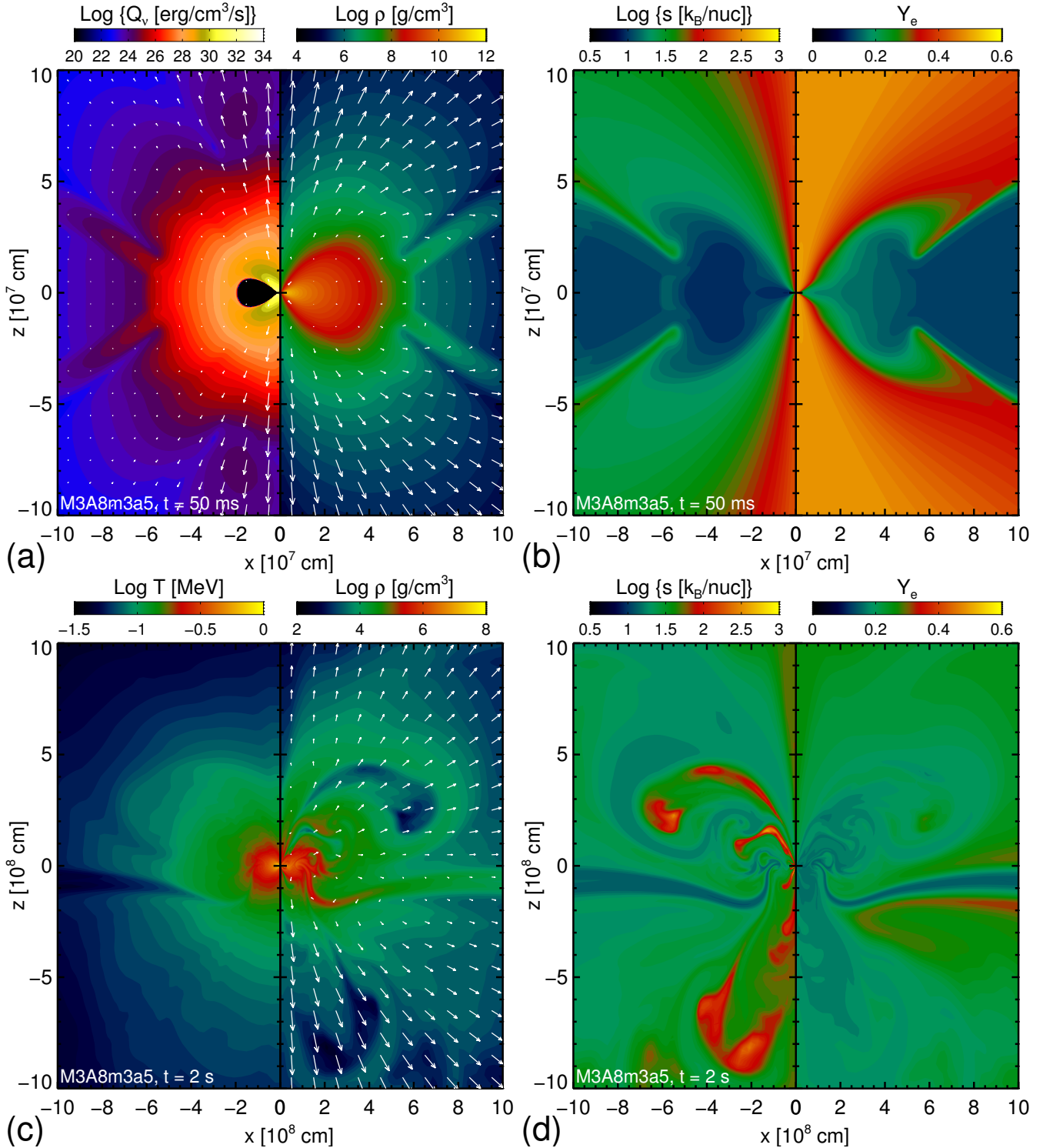


Figure 5. Snapshots for the BH-torus model M3A8m3a5 at $t = 50 \text{ ms}$ (top row) and $t = 2 \text{ s}$ (bottom row). At early times neutrino-driven ejecta dominate the outflow, whereas at late times the viscous component is more important. Plot (a) shows the total net neutrino-heating rate (left panel), overlaid with arrows indicating the vectors of the energy-integrated energy flux for electron neutrinos multiplied by $4\pi r^2$, and the density (right panel), overlaid with arrows for the velocity vectors. The neutrino-heating rate includes neutrino absorption on nucleons as well as neutrino-pair annihilation; in the black region neutrino cooling dominates heating. The maximum arrow lengths correspond to values of $5 \times 10^{53} \text{ erg s}^{-1}$ and $7 \times 10^9 \text{ cm s}^{-1}$ in the left and right panels, respectively. Plot (b) shows the entropy (left panel) and the electron fraction (right panel). Plots (c) and (d) display the same quantities as plots (a) and (b), respectively, but with the neutrino information replaced by temperature. The longest arrow in plot (c) defines a velocity of $2 \times 10^9 \text{ cm s}^{-1}$. Note that the radial scales as well as the density ranges for the plots at $t = 50 \text{ ms}$ and 2 s are different.

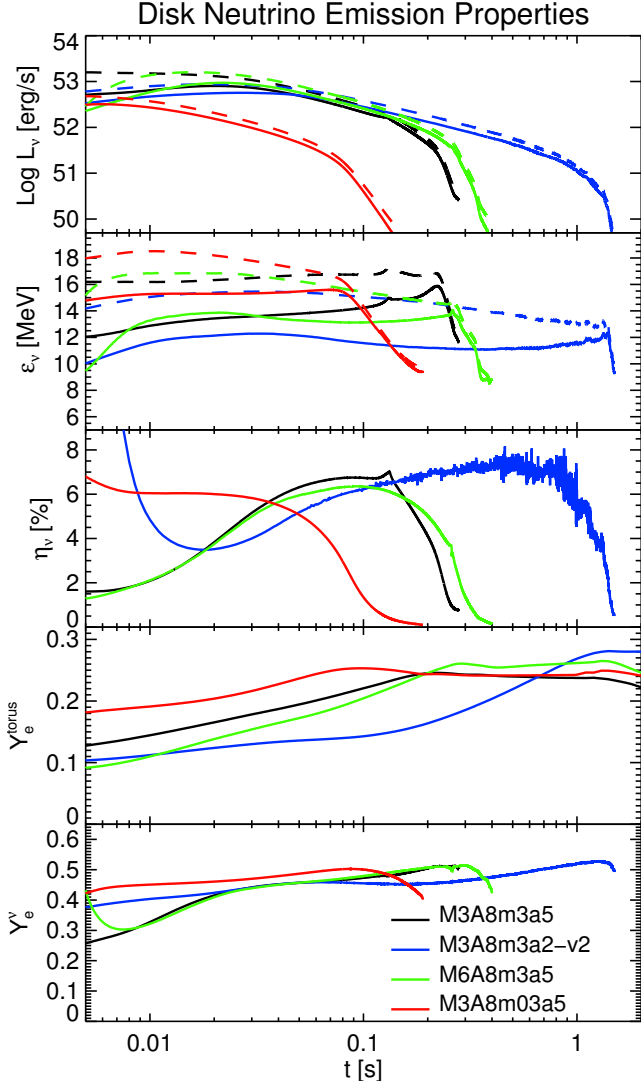


Figure 6. Time dependent neutrino emission properties for four BH-torus models. The upper two panels show the energy-integrated luminosities, L_ν , of ν_e (solid lines) and $\bar{\nu}_e$ (dashed lines) and the corresponding mean energies, ϵ_ν , respectively. The latter are defined as $\epsilon_\nu \equiv L_\nu/L_{N,\nu}$ with $L_{N,\nu}$ being the total neutrino number emission rate for neutrino ν . The values are obtained by integrating the radial components of the neutrino flux densities in the laboratory frame over a spherical surface at radius $r = 500$ km. The third panel from the top shows the neutrino-emission efficiency parameter η_ν according to Eq. (3). The fourth panel from the top gives the mean electron fractions of the tori, $Y_e^{\text{torus}} \equiv (\int dV \rho Y_e)/(\int dV \rho)$. The bottom panel displays estimates of the asymptotic electron fraction, Y_e^ν , of the neutrino-driven wind, using the results of the two top panels in Eq. (4).

driven wind and the ADAF phase, where the outflows are mainly driven by viscous effects, are indicated by vertical dashed lines for all models. Since the viscously ejected material clearly dominates in mass (cf. Table 2) and escapes with lower velocities than the fast, early neutrino wind, the transition typically coincides with a rapid increase of the outflow rate (Fig. 7, bottom panel). We stress that at times $t < t_\nu$ outflow with the characteristic properties of material accelerated by neutrino heating (see Sect. 3.3.3) is found only at

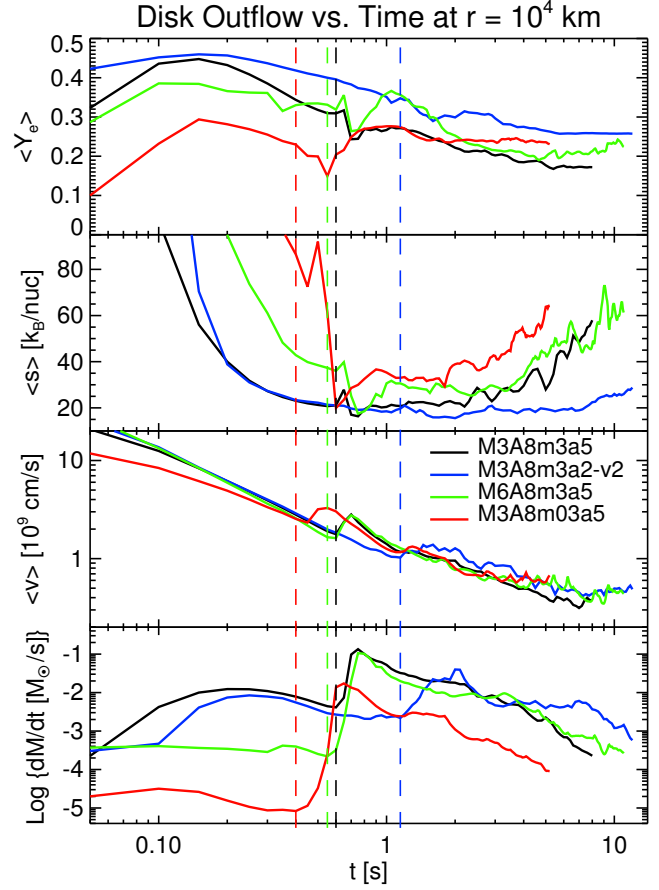


Figure 7. Outflow properties as functions of time for four BH-torus models. The upper three panels show the mass-flux weighted averages of the electron fraction, entropy, and velocity with mean value of quantity A defined as $\langle A \rangle \equiv (2\pi \int d \cos \theta A \rho v r^2)/\dot{M}_{\text{out}}$, where $\dot{M}_{\text{out}} = 2\pi \int d \cos \theta \rho v r^2$ is the total mass-outflow rate displayed in the bottom panel. All quantities are measured at a radius of $r = 10^4$ km, which implies a time retardation of roughly 0.1–1 s compared to the evolution shown in Fig. 6. For each model a vertical dashed line indicates the time t_ν which approximately marks the transition from a mainly neutrino-driven outflow to a predominantly viscously-driven outflow (see Sect. 3.3.2).

latitudes somewhat away from the equatorial plane (usually at more than 15°), while in the plane of the disk viscous transport drives the gas expansion. However, a distinction of the two ejecta components is not always unambiguously possible, because the outflows are affected both by neutrino and dissipative heating and therefore parts of them possess mixed properties.

The angular distribution of the early ($t < t_\nu$) and late ($t \geq t_\nu$) mass loss exhibits characteristic differences because of the different mass ejection dynamics of neutrino-driven and viscously driven outflows (Fig. 8). Different from nascent neutron stars, the torus is extremely nonspherical and therefore the neutrino emission and wind ejection as well as the wind properties depend strongly on the distance from the rotation axis and on the direction. Neutrino emission and mass ejection are strongest in the vicinity of the BH. While the neutrino flux is directed mainly parallel to the rotation axis (see the arrows in the left panel of Fig. 5a), the neutrino-driven wind carries away most mass at intermediate incli-

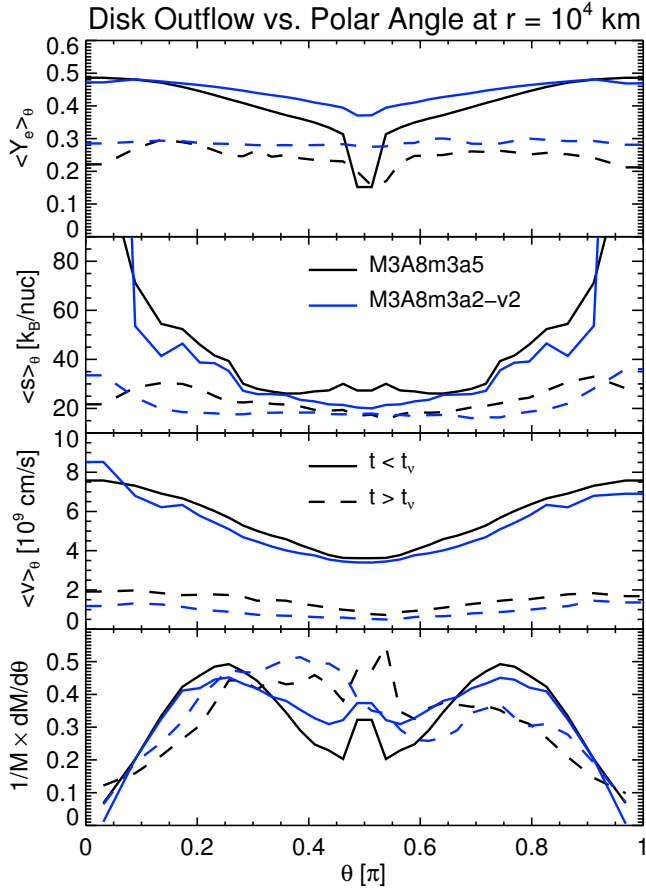


Figure 8. Polar-angle dependence of the mass ejection and ejecta properties for two representative BH-torus systems. Time-averaged quantities are shown as functions of polar angle, namely the electron fraction (top panel), entropy per baryon (second panel), and outflow velocity (third panel), all measured at a radius of 10^4 km. The bottom panel displays the differential mass loss $dM/d\theta$, normalized by the angle integral, M , of this quantity. (Note that an isotropic mass ejection corresponds to $M^{-1}dM/d\theta = 0.5 \sin \theta$.) The solid lines represent all ejecta (neutrino-driven plus viscously driven) for $t < t_\nu$ (for the meaning of t_ν , see Fig. 7), the dashed lines correspond to all ejecta for the ADAF phase, i.e., for $t \geq t_\nu$. The early ejecta include mostly neutrino-driven outflow (plus a viscously driven component near the equatorial plane at $\theta = \pi/2$) with dominant mass loss at intermediate angles. Their properties exhibit a strong dependence on the polar angle. The late ejecta contain almost exclusively viscously driven matter and are expelled much more isotropically with little variations of the outflow properties in different directions.

nation angles relative to the equatorial plane (Fig. 8). The characteristic properties (electron fraction, specific entropy, expansion velocity) of this ejecta component vary strongly with the polar angle. In contrast, the viscously driven outflows, which dominate the ejecta by far in the ADAF phase at $t \geq t_\nu$, are much more spherical and their time-averaged properties show much less angular variation (dashed lines in the panels of Fig. 8). While outward angular momentum transport perpendicular to the rotation axis drives equatorial mass loss, a considerable fraction of the viscously heated disk matter is also blown away with large angles relative to the torus equator, lifted out of the gravitational potential

by pressure forces and convective motions in the vertically inflated configuration.

The integrated mass of the neutrino-driven outflow, $M_{\text{out},\nu}$, and the total ejecta mass (neutrino plus viscosity driven), M_{out} , are listed for all simulated BH-torus models in Table 2. The total outflow mass M_{out} takes into account all material that has crossed the radius of 10^4 km until the end of the simulation⁴, while $M_{\text{out},\nu}$ includes only material that has crossed $r = 10^4$ km at times $t < t_\nu$ and at angles $> 15^\circ$ away from the equator. While the viscous outflows are a robust feature, carrying away ~ 19 – 26% of the original torus mass, the neutrino-driven wind masses are considerably smaller, with $M_{\text{out},\nu}$ reaching at most $\sim 1\%$ of the initial torus mass. Since the neutrino-wind properties are steep functions of the neutrino luminosity (cf., e.g., Qian & Woosley 1996, for the case of neutrino-driven winds of proto-neutron stars), the amount of such ejecta depends much more sensitively on the torus mass and, particularly for less neutrino-opaque tori of low mass, also on the viscosity. More massive tori and higher viscosities (which produce more heating) lead to larger neutrino luminosities.

In contrast, the fraction of the torus that is expelled in viscously driven outflows varies only weakly for different torus masses. For increasing BH mass (and all other system parameters fixed) the masses of both kinds of ejecta decrease. Two effects contribute to this decline. First, the tori around higher-mass BHs in our models are more strongly gravitationally bound, i.e., a greater part of their material possesses high specific binding energies, making it harder to lift this material out of the gravitational potential well⁵. Second, for bigger BHs the neutrino-heating efficiency, $\eta_{\nu,\text{heat}} \equiv Q_{\nu,\text{tot}} / (L_{\nu_e} + L_{\bar{\nu}_e})$ (with $Q_{\nu,\text{tot}}$ being the total net neutrino-heating rate), drops because the torus is geometrically smaller relative to the size of the BH. This reduces the “self-irradiation effect” around the axial funnel above the poles of the BH, by which neutrinos emitted from the neutrinosphere close to the BH, where the temperatures are highest, can be reabsorbed in near-surface matter at other places of the torus “walls” around the axial funnel. A torus that is big in comparison to the BH is supportive for this effect, a vertically less extended torus (or, in the extreme case, a disk) diminishes it.

A stronger neutrino-energy transfer to the medium in the outer torus layers does not only enhance the neutrino-driven wind but also the outflows caused by viscous effects. This can be seen by the additional BH-torus model M3A8m3a2-noh that we computed without net neutrino heating. In this simulation the total ejecta account for 18.7% of the initial torus mass compared to 22.3% in the corresponding model M3A8m3a2, which includes all neutrino effects. This difference is considerably larger than $M_{\text{out},\nu}$ in model M3A8m3a2, which equals only about one per cent of the torus mass. This can be understood by the fact that neutrino heating does not only drive mass ejection but also

⁴ All BH-torus models are evolved up to a time at which the sphere of radius 10^4 km contains less than one per cent of the original torus mass M_{torus} .

⁵ Note that the qualitative tendency of higher mean specific binding energies for more massive BHs is consistent with the results of our NS-BH simulations and the corresponding energy values are even in good quantitative agreement.

causes a mass flow from torus regions closer to the BH, where the heating is strongest, to more distant locations. This matter does not become unbound by neutrino-energy transfer but settles into the torus again at larger radii, partly feeding the slower viscous-outflow component from these regions. When net neutrino heating is switched off, the neutrino-aided relocation of inner torus material does not happen but this matter is accreted by the BH during the NDAF phase instead.

As mentioned above, higher values for the dynamic viscosity coefficient and the larger viscosity effects connected with the type-1 prescription increase the neutrino-driven outflows by raising the neutrino luminosities during the NDAF phase and also by improving the conditions for the neutrino self-irradiation effect. The latter is a consequence of the torus inflation in reaction to viscous heating. Enhanced viscous dissipation of kinetic energy, which instigates more violent convective mass motions in a bigger volume, as well as viscous angular momentum transport also have a direct, positive impact on the mass loss from the outer regions of the torus.

Finally, radioactive decay heating that is approximately included in two test calculations (suffix “rh” in the model names) turns out to produce negligible differences in the ejecta mass of both outflow components.

3.3.3 Ejecta properties

The nucleosynthesis-relevant ejecta properties of our four representative merger remnant models are plotted in Figs. 7 and 9. Figure 7 displays the time evolution of the mass-flux averaged electron fraction, $\langle Y_e \rangle$, entropy per nucleon, $\langle s \rangle$, and outflow velocity, $\langle v \rangle$, for all ejecta leaving a sphere of radius $r = 10^4$ km. In Fig. 9 we show the corresponding histograms of the ejecta mass distribution for Y_e , s , the dynamical expansion timescale $\tau_{\text{dyn}} \equiv r/v$ (all measured at $T = 5$ GK) and v (measured at $r = 10^4$ km), distinguishing between neutrino-driven outflow and the total (neutrino-driven plus viscously driven) mass loss. Average values of Y_e , s and v of the whole expelled matter for each of our simulated BH-torus configurations are listed in Table 2.

For both neutrino-driven and viscously driven ejecta the basic features of the time evolution of the average electron fraction, specific entropy, and expansion velocity (Fig. 7) as well as the overall properties of the mass distributions of these quantities (Fig. 9) are similar in all cases and their dependence on the investigated global parameters of the BH-torus systems is fairly weak. Overall, the neutrino-driven wind in all models is less neutron rich, has higher entropies, and expands faster than the viscous wind (Fig. 9). The bulk of the neutrino-driven wind material has $Y_e \sim 0.3$ – 0.5 , $s/k_B \sim 20$ – 50 per nucleon, τ_{dyn} around 10 ms, and asymptotic outflow velocities v significantly above 10^9 cm s $^{-1}$ up to more than 10^{10} cm s $^{-1}$. In contrast, the viscous outflows exhibit a wider spread of conditions with the maxima of the distributions being around $Y_e \sim 0.1$ – 0.35 , $s/k_B \sim 10$ – 30 per nucleon, $\tau_{\text{dyn}} \sim 100$ ms, and expansion velocities between 0.5×10^9 cm s $^{-1}$ and about 3×10^9 cm s $^{-1}$.

A lower value of the dynamic viscosity coefficient (or viscosity of type 2 instead of type 1) notably increases the average and minimum electron fractions in the viscously driven ejecta. This can be qualitatively understood from the

fact that for a slower expansion Y_e has more time to increase from its low initial values towards higher values near weak β -equilibrium in the hot, more dilute outflow. Y_e thus rises until weak beta-processes freeze out when their reaction timescale exceeds the expansion timescale, which happens earlier in faster outflows. In the case of more massive BHs, expelled matter not classified as neutrino driven develops a tail of the Y_e distribution that extends far beyond 0.5. The strength of this tail increases with the BH mass (cf. the lower left panel for model M6A8m3a5 in Fig. 9). These special ejecta are connected to a high-temperature, low-density bubble that forms in the inner torus (close to the BH) at the time when the transition from the NDAF phase to the ADAF stage takes place. The bubble accelerates outward due to buoyancy forces and for our models with BH masses $\geq 4 M_\odot$ triggers mass ejection of material whose Y_e is close to the equilibrium value on the proton-rich side.

The basic behavior of the neutron-to-proton ratio in the torus medium and in the neutrino-driven and viscously driven outflows can be understood on grounds of simple considerations (which involve physics in close analogy to what applies for matter in some regions and phases of supernova cores). During the NDAF phase, where neutrino production by electron and positron captures on free nucleons is fast but the created neutrinos are not trapped, the bulk of the torus matter resides close to neutrino-less β -equilibrium corresponding to vanishing electron neutrino chemical potential, $\mu_\nu = 0$. For typical torus densities and temperatures ($\rho \sim 10^{10}$ – 10^{12} g cm $^{-3}$ and $T \sim 10$ – 100 GK ~ 1 – 10 MeV, respectively) such conditions imply low values of the electron fraction, $Y_e^\beta \equiv Y_e(\rho, T, \mu_\nu = 0) \sim 0.1$ – 0.2 , for which electrons are moderately degenerate (see, e.g., Ruffert et al. 1997; Beloborodov 2003; Chen & Beloborodov 2007; Arcones et al. 2010).

In contrast, when the density and temperature in the expanding, neutrino-driven outflow drops, electron and positron captures, whose rates scale roughly with T^5 , freeze out quickly. Being exposed to the intense neutrino fluxes produced by the torus in the NDAF phase, however, nucleons in the cooling ejecta continue to absorb ν_e and $\bar{\nu}_e$. If these reactions achieve kinetic equilibrium, the corresponding value of the electron fraction can be approximately expressed in terms of the neutrino luminosities, L_ν , and mean energies, ε_ν , as (Qian & Woosley 1996):

$$Y_e^\nu \simeq \left(1 + \frac{L_{\bar{\nu}_e} \varepsilon_{\bar{\nu}_e} - 2Q_{\text{np}}}{L_{\nu_e} \varepsilon_{\nu_e} + 2Q_{\text{np}}} \right)^{-1}. \quad (4)$$

Here $Q_{\text{np}} \simeq 1.29$ MeV is the rest-mass energy difference between neutrons and protons. Note that ε_ν as defined in Fig. 6 differs from the mean energy that appears in the derivation of Y_e^ν by Qian & Woosley (1996), but the numerical estimate of Y_e^ν is very similar. The lower panel of Fig. 6 shows our estimates of Y_e^ν as functions of time for four representative BH-torus systems, whose neutrino luminosities and mean energies are displayed in the top two panels of this figure. The values of $Y_e^\nu \sim 0.3$ – 0.5 are considerably higher than in the torus itself and in the same ballpark as those obtained for the neutrino-driven outflows in the hydrodynamical simulations (cf. top panel of Fig. 7; note the retardation time of ~ 0.1 – 1 s that needs to be taken into account in comparing Figs. 7 and 6). Of course, more than rough qualitative agreement cannot be expected because Eq. (4) provides only

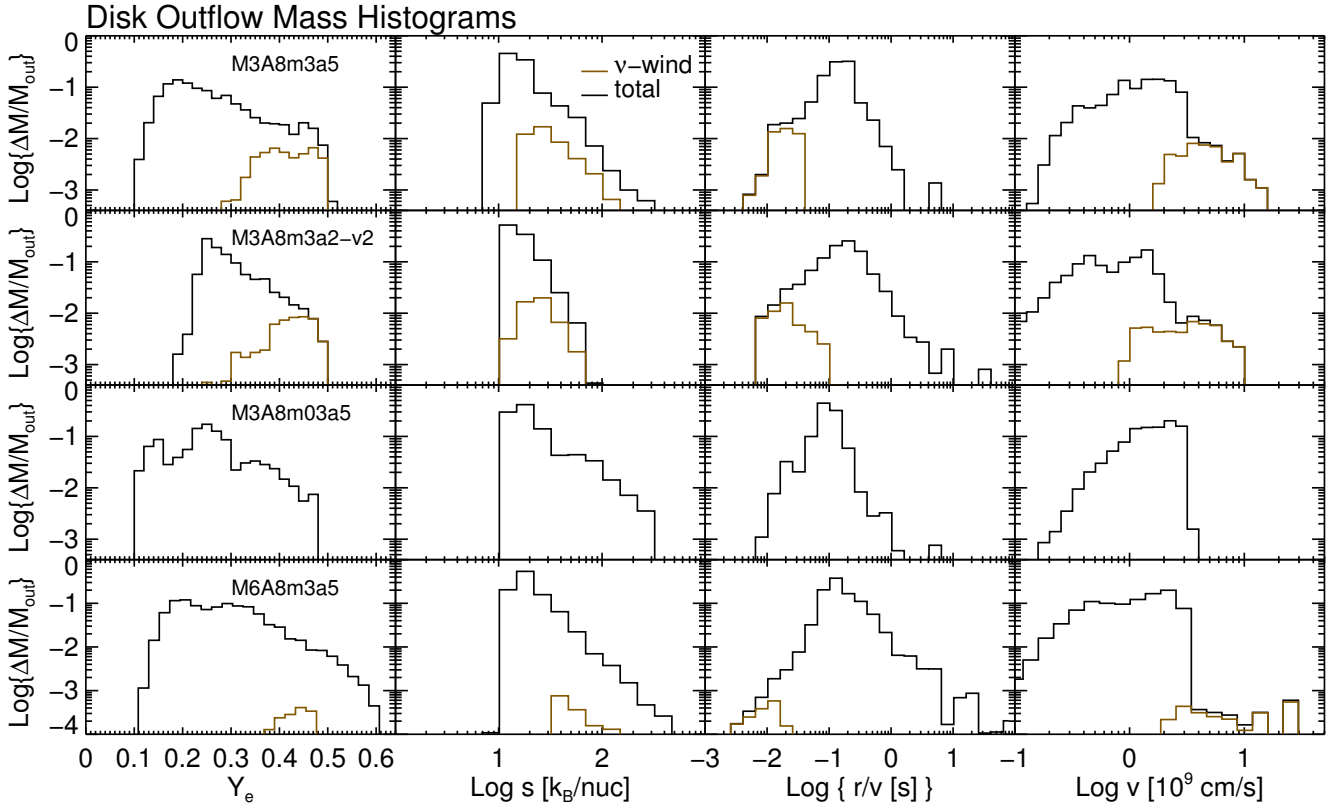


Figure 9. Mass-distribution histograms of the neutrino-driven outflow (brown lines) and of the whole (neutrino-driven plus viscously driven) ejecta (black lines) for the four representative BH-torus models named in the left panels. All distributions are normalized by the total mass, M_{out} , expelled in each case. From left to right the panels show the distributions for electron fraction, entropy per nucleon, dynamical expansion timescale, and velocity. The first three quantities are measured at the time when the temperature of an escaping fluid element has dropped to 5 GK, the outflow velocities are measured at a fixed radius of $r = 10^4$ km.

a crude estimate. On the one hand it assumes the neutrino luminosities to be radiated isotropically while the neutrino fluxes emitted by the accretion tori depend strongly on the direction and position. On the other hand the assumption of kinetic equilibrium of ν_e and $\bar{\nu}_e$ absorptions breaks down when the wind expansion becomes too fast, in which case the electron fraction in the wind freezes out at a value lower than Y_e^ν . This is most obvious in the case of model M3A8m03a5 with its low torus mass and correspondingly low neutrino luminosities, where $\langle Y_e \rangle$ in the neutrino-driven ejecta hardly climbs up to 0.3 (Fig. 7, top panel).

Despite similarities in the dynamics and thermodynamics of neutrino-driven and viscously driven outflows the conditions that determine their nuclear composition are drastically different. At the end of the NDAF phase the neutrino emission becomes so low that neutrino absorption does not play a role any longer. Instead, during the ADAF stage e^\pm -captures drive the electron fraction in the outflowing material towards the local equilibrium value given by $Y_e^\beta(\rho, T, \mu_\nu = 0)$. Because the electron degeneracy in the warm, dilute outer torus regions is low, the neutron-proton mass difference suppresses electron captures on protons compared to positron captures on neutrons, for which reason one expects $Y_e^\beta > 0.5$. Nevertheless, the true electron fractions computed for the ejecta during the ADAF phase usually remain clearly on the neutron-rich side (except in the matter ejected in hot, buoyant bubbles at the transition from the

NDAF to the ADAF stage, see above). This is explained by the fact that the torus expands and cools by viscous effects during the ADAF evolution. The rates of e^\pm -captures therefore decrease continuously and Y_e in the torus and outflow freezes out when the viscous timescale becomes shorter than the capture timescales of electrons and positrons (e.g., Metzger et al. 2009). In agreement with Metzger et al. (2009) and Fernández & Metzger (2013) we find that much of the viscously driven ejecta remain very neutron rich with $Y_e \sim 0.15$ – 0.25 , but some fraction develops higher Y_e (see Fig. 9, left panels) so that the average values are more around $Y_e \sim 0.2$ – 0.3 (cf. Fig. 7, top panel, and Table 2).

3.3.4 Comparison with Fernández & Metzger (2013)

The basic evolutionary features of the models described here are similar to those found by Fernández & Metzger (2013). However, the outflow properties we obtain exhibit some differences in important details. Fernández & Metzger (2013) made use of a much simpler neutrino treatment than ours, which essentially prevented them from modeling systems in which significant neutrino-driven winds can be expected.

In a test simulation with a nonrotating BH corresponding to model S-def investigated by Fernández & Metzger (2013), we find that roughly 8% of the torus mass leave a sphere of 10^4 km almost exclusively as viscously driven outflow, but only a fraction of this mass (4–8% of the torus

mass) fulfills the criterion that the total (internal plus kinetic plus gravitational) specific energy is positive when crossing the radius of 10^4 km. This criterion is employed to estimate the actual amount of material that will finally become gravitationally unbound and be mixed into the interstellar medium. However, since thermal effects are still dynamically relevant at $r = 10^4$ km, the criterion depends on the thermal energy that ultimately contributes to unbind the outflow, i.e., on the normalization of the internal energy used to evaluate the criterion at $r = 10^4$ km. In our test simulation we obtained the lower estimate of the unbound outflow mass ($\sim 4\%$ of the torus mass) when taking for the internal energy the thermal energy instantly resulting from our 4-species EOS at $r = 10^4$ km, while we determined almost all of the outflow as nominally unbound when assuming that the thermal energy at $r = 10^4$ km corresponds to all nucleons being recombined with an average nuclear binding energy of 6 MeV per nucleon⁶. Fernández & Metzger (2013) quoted a fraction of 10% of the initial torus mass to become unbound, which, however, was reassessed by (Metzger & Fernández 2014) as being too large by a factor of \sim few due to an erroneous overestimation of the recombination heating by α particles. Hence, without having more detailed published information available for now, we consider our masses of unbound outflows to be approximately consistent with Fernández & Metzger (2013). An interesting feature worth to record from the comparison with Fernández & Metzger (2013) is that the BH spin appears to have a sizable impact on the amount of ejecta produced by the disk.

While the ejecta masses seem to be in reasonable agreement, the bulk of the outflow in the model of Fernández & Metzger (2013) is slightly more neutron rich, $Y_e \sim 0.1\text{--}0.21$, than in our simulation, $Y_e \sim 0.18\text{--}0.30$. The reason of this difference cannot be unambiguously identified. The lower values of Y_e could simply also be a consequence of the error in the α -recombination heating, leading to higher escape velocities and therefore faster freeze-out from weak-reaction equilibrium. However, Metzger & Fernández (2014) mention that the changes of nucleosynthesis-relevant properties associated with their mistake are irrelevant. Another possible reason for the Y_e difference could be connected to the different treatments of neutrino reactions and transport.

3.4 Nucleosynthesis

3.4.1 Nucleosynthesis in the dynamical ejecta

The nucleosynthesis resulting from the dynamical ejecta has been studied previously either based on parametrized ejecta trajectories (Freiburghaus et al. 1999; Goriely et al. 2005) or more “realistic” hydrodynamical Newtonian (Korobkin et al. 2012; Rosswog et al. 2014) and (CFC-) relativistic (Goriely et al. 2011b; Bauswein et al. 2013b; Goriely et al. 2013) simulations of NS-NS binary systems, recently also including neutrino effects in relativistic merger models (Wanajo et al. 2014). In all these simulations, the number of free neutrons per seed nucleus reaches a few hundred.

⁶ In our models with $A_{\text{BH}} = 0.8$, typically $\gtrsim 90\%$ of the material that reaches a radius of more than 10^4 km are nominally unbound independent of the precise energy normalization, and we therefore count all mass at $r > 10^4$ km as ejecta.

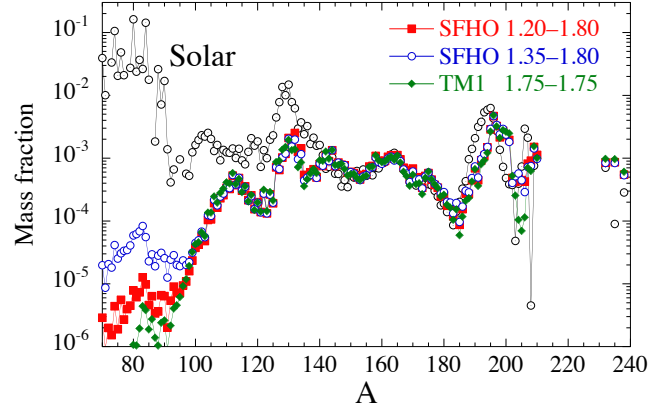


Figure 10. Abundance distributions as functions of the atomic mass for the dynamical ejecta of three NS merger cases with prompt collapse of the remnants. Each binary system is characterized in the legend by the EOS used in the simulation and the mass (in M_{\odot}) of the two NSs. All distributions are normalized to the same $A = 196$ abundance. The dotted circles show the solar r-abundance distribution (Goriely 1999).

With such a neutron richness, fission plays a fundamental role by recycling the matter during the neutron irradiation and by shaping the final r-abundance distribution in the $110 \lesssim A \lesssim 170$ mass region at the end of the neutron irradiation. Thanks to this property, the final composition of the ejecta is rather insensitive to details of the initial abundances and the astrophysical conditions, in particular the mass ratio of the two NSs, the quantity of matter ejected, and the EOS (Goriely et al. 2011b; Bauswein et al. 2013b; Korobkin et al. 2012). The mentioned calculations essentially correspond to the delayed-collapse scenario and their typical yields are displayed in Fig. 11. In the following we present our first nucleosynthesis results obtained for cases with prompt collapse of the NS-NS binary merger remnant as well as for NS-BH binary systems (cf. Table 1).

Prompt collapse cases

Figure 10 shows the abundance distributions resulting from the prompt collapse of NS-NS binary systems. The three cases exhibit similar pattern characteristics of the fission recycling nucleosynthesis, as described in Goriely et al. (2013, 2014). In the relativistic simulations, in contrast to the Newtonian approximation (where ejecta originate mostly from cold extended spiral arms; Korobkin et al. 2012; Rosswog et al. 2014), not all the mass elements lead to the same composition after ejection. Mass elements are ejected with considerably different velocities so that the density evolution may vary significantly from one trajectory to the next (cf. Bauswein et al. 2013b). Fast expanding mass elements might not have time to capture all available free neutrons leading to no or only one fission cycle while more slowly expanding mass elements allow for all free neutrons to be captured and typically three fission cycles to take place (Goriely et al. 2014).

Delayed collapse cases

In the delayed collapse cases, the integrated mass associated with rapidly expanding material compared to the total ejecta mass remains relatively smaller than in the prompt collapse cases. For this reason, similar to Newtonian mod-

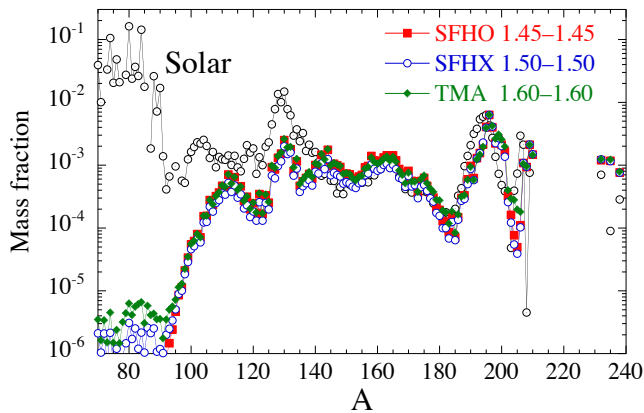


Figure 11. Abundance distributions as functions of the atomic mass for the dynamical ejecta of three NS merger cases with delayed collapse of the remnants. Each binary system is characterized in the legend by the EOS used in the simulation and the mass (in M_{\odot}) of the two NSs. All distributions are normalized to the same $A = 196$ abundance. The dotted circles show the solar r-abundance distribution (Goriely 1999).

els of the NS-merger hydrodynamics, which tend to predict rather slow expansion (Korobkin et al. 2012), the abundance distributions of relativistic models with delayed remnant collapse exhibit a trough around $A \simeq 200$ (Fig. 11). This deep trough is absent in the prompt collapse cases (Fig. 10), where the relative contributions of quickly expanding trajectories to the final abundance distribution are found to be appreciable and to fill the trough in the $A \simeq 200$ region.

Comparison between NS-NS and NS-BH nucleosynthesis

Figure 12 illustrates the abundance distributions representative of three NS-BH binary systems. In the NS-BH cases, the expansion velocities are rather low (see Table 1), comparable to the delayed collapse cases of the NS-NS systems and lower than those in the prompt collapse cases. The corresponding abundance distributions are therefore rather similar to those found in the NS-NS delayed collapse with an underproduction of the $A \simeq 202$ nuclei.

Impact of neutrinos

During the binary merging phase we disregard the effects of neutrinos in our hydrodynamic simulations as well as in the nucleosynthesis studies. In a few recent simulations with nucleosynthesis discussion neutrino effects were explored. While Korobkin et al. (2012) did not find a significant impact in their Newtonian studies, the relativistic NS-NS merger calculations of Wanajo et al. (2014) for a “soft” nuclear EOS (i.e., neutron stars with small radii) point towards a substantial impact of neutrino reactions on the electron fraction Y_e in the dynamical ejecta of cases with delayed collapse of the merger remnant. While positron captures on the abundant neutrons in shock-heated matter stripped by the neutron stars must be expected to raise Y_e , Wanajo et al. (2014) also reported an additional Y_e increase by electron neutrino absorption in escaping ejecta. In essence, these weak interactions widen the distribution of Y_e in the outflow such that in addition to heavy r-process elements ($A > 140$) also nuclei with lower mass numbers are created. It is still unclear whether the observed effects apply similarly strongly to all high-density EOSs and all binary systems that lead to

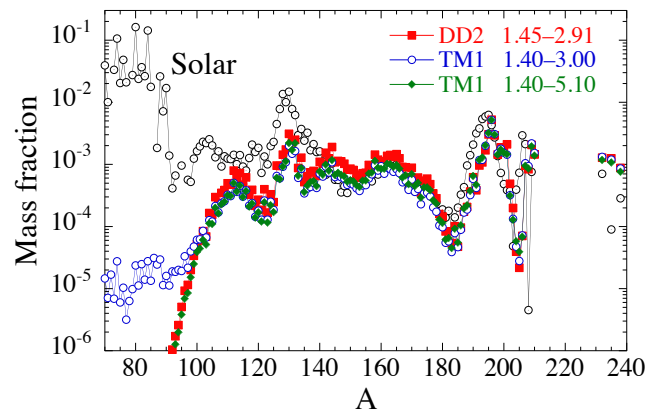


Figure 12. Abundance distributions as functions of the atomic mass for the dynamical ejecta of three NS-BH merger cases. Each binary system is characterized in the legend by the EOS used in the simulation and the mass (in M_{\odot}) of the NS and BH, respectively. All distributions are normalized to the same $A = 196$ abundance. The dotted circles show the solar r-abundance distribution (Goriely 1999).

a delayed collapse of the merger remnant. Also the prompt collapse scenario and NS-BH mergers have not yet been investigated in all relevant aspects in this context. The impact of neutrinos may be less important in the latter two cases, because mass ejection there can be faster and more immediate so that strong shock heating (associated with violent pulsations of the compact remnant or the collision of torus matter with itself) affects only a smaller fraction of the ejecta, and because of the absence of a hot, massive central object emitting copious neutrinos. For NS-BH mergers this expectation seems to receive confirmation by recent results in Foucart et al. (2014).

In any case, the simulations by Wanajo et al. (2014) confirm that the dynamical ejecta are a robust source of heavy r-process nuclei, but in addition may also produce a contribution to r-process material with $A < 140$. The relative amounts of nuclei above and below $A \sim 140$, however, are massively affected by the long-lasting mass loss from the merger remnant that follows the immediate ejection of material during the merging phase and early afterwards. As we will demonstrate below for BH-torus systems, the final nucleosynthetic abundance distribution depends strongly on the detailed properties of the BH-torus configuration and the spatial asymmetry of the ejecta expelled by the binary merger and post-merger remnant.

3.4.2 Nucleosynthesis in the disk ejecta

In modeling the hydrodynamics and nucleosynthesis of the remnant ejecta, we consistently included the electron and positron captures on free nucleons as well as the inverse captures of electron neutrinos and antineutrinos. Note that the neutrino absorption rates (per nucleon) as obtained in the hydrodynamic torus simulations were provided as functions of time along the tracer trajectories for all nucleosynthetically processed mass elements of the ejecta. This procedure ensured that the asymmetry of the neutrino emission was taken into account in its effects on the element formation.

Neutrino-driven and viscous components

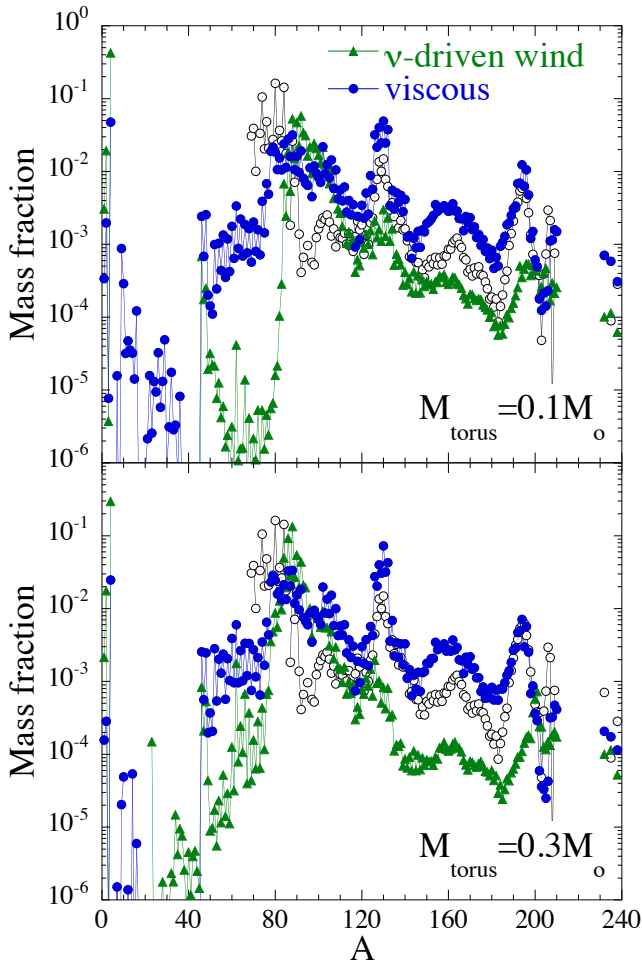


Figure 13. Abundance distributions as functions of the atomic mass for the neutrino-driven and viscous components of the disk ejecta for tori of $0.1 M_{\odot}$ (top) and a $0.3 M_{\odot}$ (bottom). All distributions are normalized so that $\sum_X = 1$. Calculations correspond to the M3A8m1a5 and M3A8m3a5 models. The dotted circles show the solar r-abundance distribution (Goriely 1999).

The neutrino-driven and viscous outflow components identified in Sect. 3.3 are characterized by different properties, i.e., the neutrino-driven component exhibits larger average electron fractions and higher escape velocities (cf. Fig. 9 and Sect. 3.3.3). Consequently, the abundance patterns are different with less strong r -processing in the neutrino-driven ejecta (Fig. 13). In the neutrino-driven wind, the trajectories with electron fractions $Y_e \lesssim 0.35$ and with the shortest expansion timescales can still be responsible for the production of the heavy r -nuclei with $A > 140$. In the viscous ejecta, the average electron fraction is sufficiently lower such that the third abundance peak is reached for a substantial amount of outflow trajectories. In all studied cases, the mass of the neutrino-driven outflow remains small compared to the one associated with the viscous component (cf. Table 2). The final, ejected (combined) abundance distribution in the disk outflows is therefore essentially identical to the viscous component. The ejected matter is roughly composed of 80 to 94% of r -process material, the remaining 6 to 20% being made essentially of ${}^4\text{He}$.

Sensitivity to global parameters

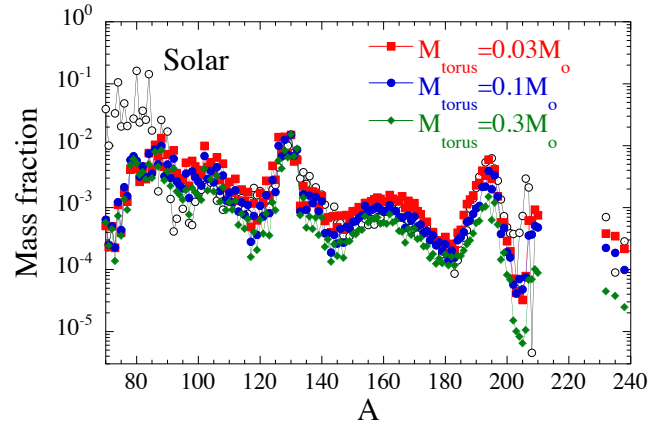


Figure 14. Abundance distributions as functions of the atomic mass for three systems with torus masses of $M_{\text{torus}} = 0.03, 0.1$ and $0.3 M_{\odot}$ and a $3 M_{\odot}$ BH. All distributions are normalized to the same solar $A = 130$ abundance. Calculations correspond to the M3A8m03a5, M3A8m1a5 and M3A8m3a5 models. The dotted circles show the solar r -abundance distribution (Goriely 1999).

The abundance distributions are found to be only weakly sensitive to the torus mass, as shown in Fig. 14 for cases with the same BH mass and spin and the same viscosity. The differences result from the two subtle trends that the fraction of material with $Y_e < 0.2$ as well as the mean entropy slightly increase for lower torus masses. As can be seen in Fig. 15, the abundance distribution is also found to be only moderately sensitive to the BH mass. The observed slight trend towards relatively heavier elements for lower BH masses can be ascribed to the lower mean electron fractions of the ejecta. In Fig. 16, we compare the abundance distributions obtained with two values of the viscosity parameter α_{vis} , both for the type 1 and type 2 prescriptions, as described in Sect. 2.2. In general terms, the abundance distribution is quite robust with respect to the viscosity treatment for the intermediate-mass elements $80 \leq A \leq 130$, while it is rather sensitive to the viscosity for the $A > 130$ elements. We observe that for a higher dynamic viscosity coefficient η_{vis} a higher relative amount of $A > 130$ elements is obtained (remembering also that the η_{vis} for the two viscosity types are related by Eq. 2). This result can be explained by the fact that a higher dynamic viscosity leads to a smaller mean electron fraction \bar{Y}_e of the ejecta in our models (cf. Table 2).

Sensitivity to r -process heating feedback

In Fig. 17 we compare the average temperatures as well as the average heating rates for the models with and without radioactive heating as implemented by the approximate method described in Sect. 3.1. Correspondingly, in Fig. 18 we compare the abundance distributions for these models. The variations introduced by such a lowest-order correction for radioactive heating are only marginal. Besides minor differences in the abundance distributions, also the total ejecta masses are hardly affected. With heating M_{out} increases from 22.1 to 22.4 per cent and from 22.7 to 22.8 per cent of the original torus mass for models M4A8m3a5 and M3A8m1a2, respectively (see Table 2). This indicates that including the radioactive heating in a fully consistent manner is not necessary or at least does not lead to any signifi-

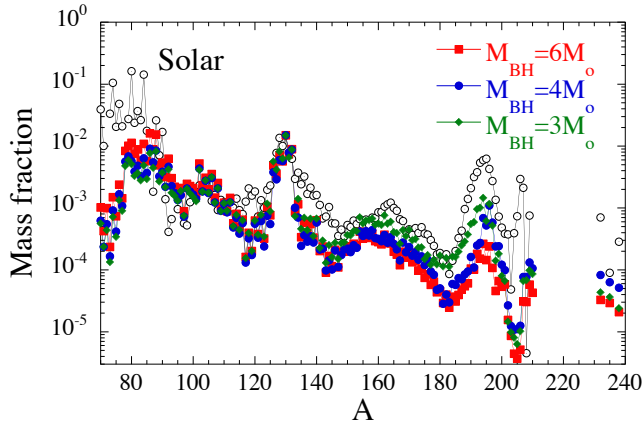


Figure 15. Abundance distributions as functions of the atomic mass for three BH-torus systems with BH masses of $M_{\text{BH}} = 3, 4$ and $6 M_{\odot}$ and the same $0.3 M_{\odot}$ tori. All distributions are normalized to the same solar $A = 130$ abundance. Calculations correspond to the M3A8m3a5, M4A8m3a5 and M6A8m3a5 models. The dotted circles show the solar r-abundance distribution (Goriely 1999).

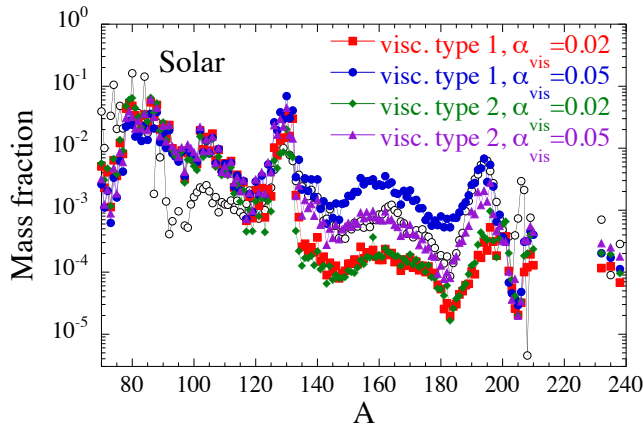


Figure 16. Abundance distributions as functions of the atomic mass for four identical BH-torus systems ($M_{\text{BH}} = 3 M_{\odot}$; $A_{\text{BH}} = 0.8$; $M_{\text{torus}} = 0.3 M_{\odot}$) computed with two different values of the viscosity parameter α_{vis} , namely $\alpha_{\text{vis}} = 0.02$ and $\alpha_{\text{vis}} = 0.05$, and two different prescriptions of the viscosity tensor (cf. Sect. 3.1). All distributions are normalized so that $\sum_X = 1$. Calculations correspond to the M3A8m3a2, M3A8m3a5, M3A8m3a2-v2 and M3A8m3a5-v2 models. The dotted circles show the solar r-abundance distribution (Goriely 1999).

cant changes of our modeling predictions (see also Rosswog et al. 2014, where a similar conclusion was drawn concerning the dynamical ejecta).

3.4.3 Combined nucleosynthesis in the dynamical and disk ejecta

Assuming that the dynamical and disk nucleosynthesis components are both ejected isotropically, we can combine the yields by summing up the mass fractions for both components, weighted by their corresponding total ejected masses. We only combine systems corresponding to the same BH mass and spin and the same torus mass in a roughly consistent manner. For models with $0.03, 0.1$ and $0.3 M_{\odot}$ tori, the

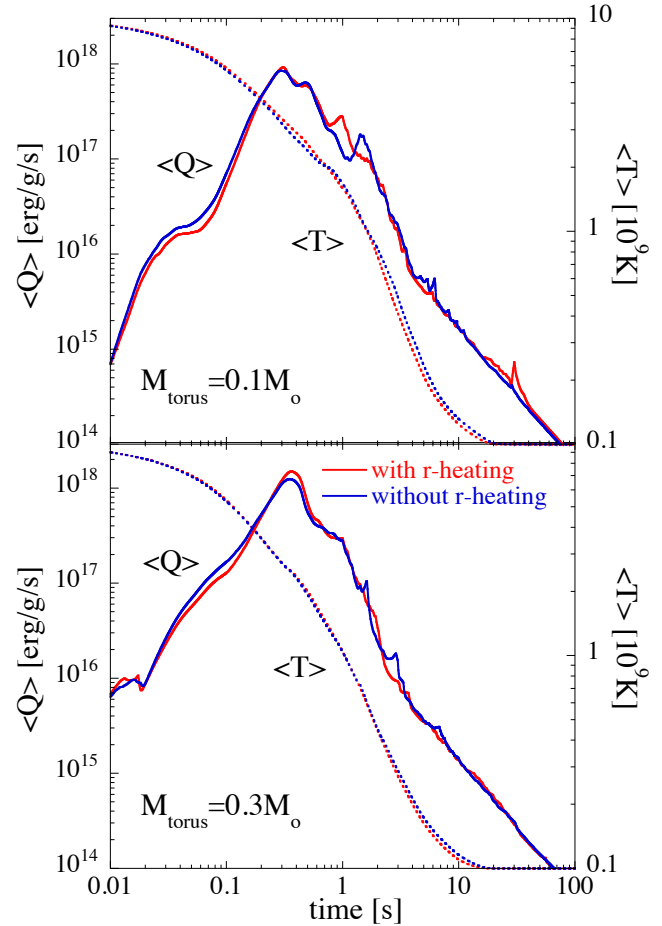


Figure 17. Time evolution of the average radioactive heating rate per unit mass, $\langle Q \rangle$, for two BH-torus systems with $M_{\text{BH}} = 3 M_{\odot}$, $A_{\text{BH}} = 0.8$, $M_{\text{torus}} = 0.1 M_{\odot}$ (top) and $M_{\text{BH}} = 4 M_{\odot}$, $A_{\text{BH}} = 0.8$, $M_{\text{torus}} = 0.3 M_{\odot}$ (bottom), when the heating feedback due to the r-process β -decays and fission is included or not. Calculations correspond to models M3A8m1a2, M3A8m1a2-rh, M4A8m3a5 and M4A8m3a5-rh.

abundance distributions for such combined models are given in Fig. 19. The dynamical ejecta contribute mainly to the production of the $A > 140$ nuclei, whereas the disk ejecta produce mostly the $90 \leq A \leq 140$ nuclei. The combined distribution is in surprisingly good agreement with the solar system r-abundance distribution (Fig. 19). However, the relative strength of the second to the third r-process peak depends sensitively on the ratio between the amount of mass ejected from the disk and the one ejected dynamically (both components being composed of about 80–98% of r-process material). For the three cases shown in Fig. 19, this ratio amounts to 1.4, 5.3 and 1.7 for the $0.03, 0.1$ and $0.3 M_{\odot}$ torus models, respectively. For this reason, when normalizing to the $A = 196$ abundance, the lighter elements, and in particular the $A \simeq 130$ peak, are found to typically vary within a factor of 3.

Note that it is well known that calculations of the r-process abundances are still affected by large nuclear physics uncertainties (Arnould et al. 2007). Such uncertainties have been extensively studied in the past, but each site provides its specific conditions and behaves in its own special manner so that an assessment of the sensitivity to theoretical

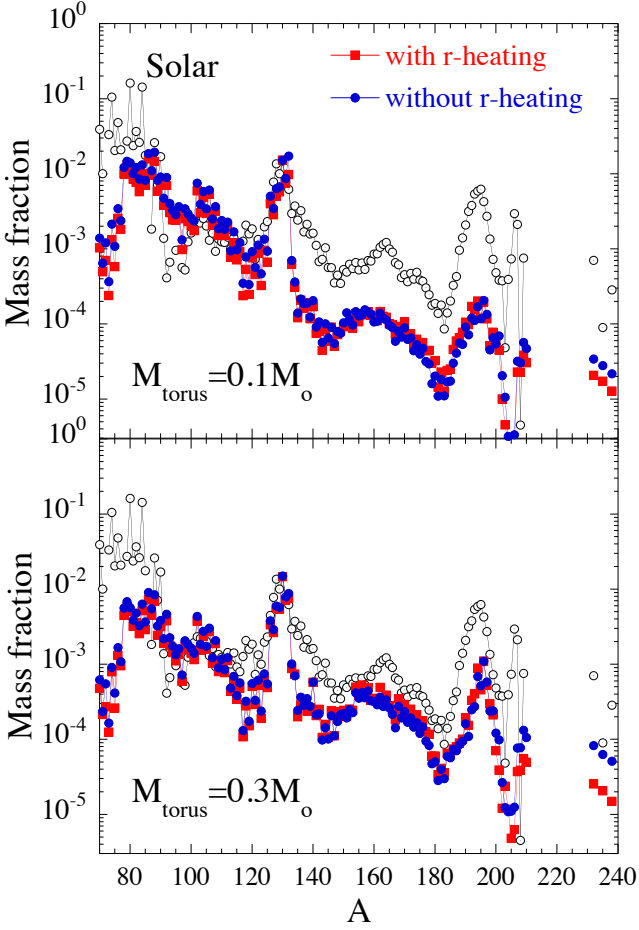


Figure 18. Abundance distributions as functions of the atomic mass for two BH-torus systems with $M_{\text{BH}} = 3 M_{\odot}$, $A_{\text{BH}} = 0.8$, $M_{\text{torus}} = 0.1 M_{\odot}$ (top) and $M_{\text{BH}} = 4 M_{\odot}$, $A_{\text{BH}} = 0.8$, $M_{\text{torus}} = 0.3 M_{\odot}$ (bottom), when the heating feedback due to the r-process β -decays and fission are included or not. All distributions are normalized to the same solar $A = 130$ abundance. Calculations correspond to models M3A8m1a2, M3A8m1a2-rh, M4A8m3a5 and M4A8m3a5-rh. The dotted circles show the solar r-abundance distribution (Goriely 1999).

nuclear physics input requires careful and dedicated exploration. While we already partly investigated the sensitivity of the nucleosynthesis in the dynamical ejecta to masses, β -decay rates, and fission probabilities (Goriely et al. 2013), we defer such a sensitivity analysis for the composition of the disk ejecta to a future study.

4 COMPARISON WITH OBSERVATIONS

The striking similarity between the solar distribution of r-element abundances in the $56 \leq Z \leq 76$ range and the corresponding abundance pattern observed in ultra-metal-poor stars like CS 22892-052 (Sneden et al. 2003, 2008, 2009) led to the conclusion that any astrophysical event producing r-elements gives rise to a solar system r-abundance distribution, at least for elements above Ba. In such r-process-enriched low-metallicity stars, some variation of about 0.5 dex, however, is found for the elements lighter than Ba. The amazingly robust r-process for elements above Ba could

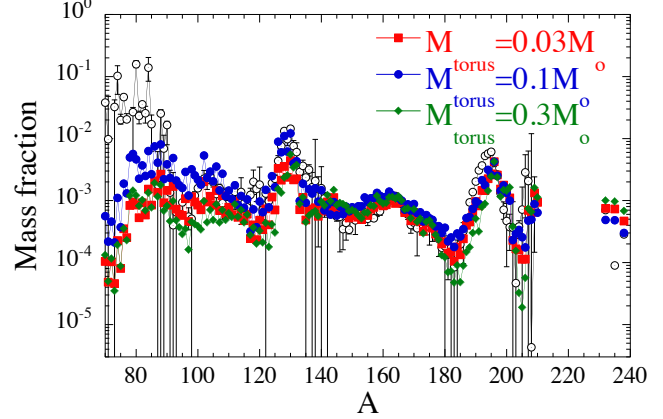


Figure 19. Abundance distributions as functions of the atomic mass for three combined systems (merger model plus remnant model) corresponding to models with torus masses $M_{\text{torus}} = 0.03, 0.1$ and $0.3 M_{\odot}$. All distributions are normalized to the same solar $A = 196$ abundance. Calculations correspond to the model combinations TMA_1616–M3A8m03a5, SFHO_13518–M3A8m1a5 and DD2_14529–M4A8m3a5. The dotted circles show the solar r-abundance distribution (Goriely 1999).

point to the possible creation of these elements by fission recycling in dynamical NS-NS or NS-BH merger ejecta, as already argued in previous studies (e.g., Goriely et al. 2011b). As seen in Fig. 19, variations of the abundances of the lighter elements with $40 \leq Z \leq 56$ relative to those of the heavier elements by factors of a few could be accounted for when the contributions of the disk ejecta in dependence on different torus masses are considered. Figure 20 shows that the elemental distribution observed in the ultra-metal-poor star CS22892-052 (Sneden et al. 2003) can be fairly well reproduced by the nucleosynthesis from the combined dynamical and disk ejecta. Discrepancies are found around the Os elements due to the shift of the third r-process peak (see Fig. 19), the exact position of which is affected by nuclear uncertainties.

Recent observations also indicate that star to star variations in the r-process content of metal-poor globular clusters may be a common, although not ubiquitous, phenomenon (Roederer et al. 2010; Roederer 2011). Stars such as HD 88609 or HD 122563 have been found to be significantly deficient in their heavy elements (Honda et al. 2007). CS 22892-052 and HD 122563 are now interpreted as two extreme cases representative of a continuous range of r-process nucleosynthesis patterns (Roederer et al. 2010).

In the previous comparison with CS22892-052 we determined the combined composition of all ejecta components by weighting both the dynamical and disk contributions by their respective total ejected masses. However, it cannot be excluded that the mass of the dynamical ejecta contributing to the final composition is in fact significantly smaller, in particular when considering NS-BH systems. Two different effects could suppress the dynamical ejecta relative to the torus ejecta. (1) As discussed in Sect. 3.2, the dynamical ejecta of NS-BH mergers can be highly asymmetric, because most of these ejecta may consist of the matter shed off the outer tip of the tidally stretched NS at its final approach to the BH. In contrast, the remnant ejecta are more isotropic. The combination of both can therefore be

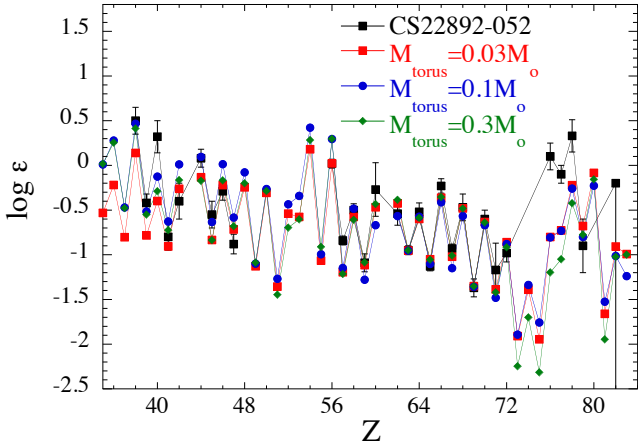


Figure 20. Comparison between the elemental abundances of CS22892-052 (in the usual logarithmic scale relative to hydrogen, $\log \varepsilon = \log_{10}(N_A/N_H) + 12$ for element A and number density N_A) and those obtained for the three combined systems corresponding to remnants with 0.03, 0.1 and $0.3 M_\odot$ tori as shown in Fig. 19. All distributions are normalized to the observed Eu abundance. Calculations correspond to the model combinations TMA_1616–M3A8m03a5, SFHO_13518–M3A8m1a5 and DD2_14529–M4A8m3a5.

strongly direction dependent. For the values of the asymmetry parameter B_{asy} given in Table 1 (cf. Sect. 3.2), the mass of the dynamical ejecta could be 20–100 times smaller than the mass of the disk ejecta outside of the solid angle of the main dynamical mass stripping. (2) Potentially, NS-BH mergers might produce little dynamical ejecta material for certain binary parameters while still forming a torus. This hypothetical possibility might exist in cases where the NS is nearly completely and immediately accreted by the BH, in which case the tidal sling effect leading to mass ejection from an extremely stretched NS might be absent. In such systems, the ejecta would consequently be essentially composed of disk material. If we assume that the contribution of the dynamical ejecta represents only about 1% of the total ejected mass, the composition of the ejecta becomes strongly depleted in heavy r-process material in comparison to the standard cases shown in Figs. 19 and 20. Such specific system conditions could qualitatively explain the composition of stars like HD 88609 or HD 122563, as shown in Fig. 21. We consider this as an interesting, speculative possibility, but the relative frequency of such possible events as well as the possible variation of the mix between the dynamical and disk contributions will need to be assessed in a more quantitative way in future studies.

5 SUMMARY, DISCUSSION, AND CONCLUSIONS

We have performed the first comprehensive study of r-process nucleosynthesis in merging NS-NS and NS-BH binaries, also including the neutrino and viscously driven outflows from BH-torus systems as remnants of the compact star mergers. Our focus was on such relic systems because they are the generic outcome of NS-BH mergers when the BH/NS mass ratio is not too large, and for NS-NS mergers in cases where the massive remnant cannot be stabilized by

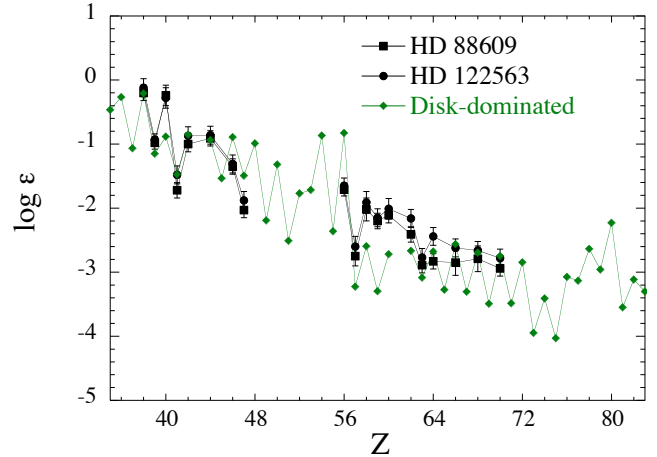


Figure 21. Comparison between the HD88609 and HD122563 elemental abundances (in $\log \varepsilon$ scale) and those estimated for the combination of models SFHO_1123 and M3A8m3a2, when the ejected mass of the dynamical component is assumed to be 100 times smaller than the one coming from the disk component. The calculated distribution is normalized to the Sr abundance of HD88609.

the NS EOS. We therefore considered binary NSs that either led to BH formation directly when the two stars plunged into each other, or produced a remnant that collapsed to a BH within less than about 10 ms for the nuclear EOSs employed in our work.

The binary mergers were simulated in 3D with a relativistic SPH hydrodynamics code, using the CFC approximation for the spacetime (Oechslin et al. 2007; Bauswein 2010) and four different microphysical EOSs for non-zero temperature NS matter (all consistent with astrophysical, experimental and theoretical bounds). The subsequent evolution of the BH-torus systems was computed over periods of up to more than 10 seconds in 2D (axisymmetry) with a Newtonian, finite-volume Godunov-type code (Obergaullinger 2008) including viscosity terms with a Shakura-Sunyaev α -prescription for the dynamic shear viscosity coefficient (Shakura & Sunyaev 1973). The gravitational field of the relic BH was described by an Artemova-Bjoernsson-Novikov potential (Artemova et al. 1996), and the neutrino transport in the accretion torus was treated by a 2D, fully energy dependent two-moment scheme with an algebraic closure for the variable Eddington tensor (Just et al., in preparation).

Although the binary-merger and remnant modeling were not carried out continuously and not fully consistently, we ensured compatibility of both evolution phases by connecting the investigated BH-torus models with NS-NS and NS-BH binaries that produced remnants with the same (or at least very similar) BH masses ($M_{\text{BH}} \approx 3, 4, 6 M_\odot$), torus masses ($M_{\text{torus}} \approx 0.03, 0.1, 0.3 M_\odot$), and BH spins ($A_{\text{BH}} \approx 0.8$). Starting with tori in rotational equilibrium minimized artificial transients. The action of viscous angular momentum transport and redistribution establishes quasi-stationary accretion typically within 10–20 ms, and dissipative viscous heating and fast electron and positron captures on free nucleons quickly (within <10 ms) drive the initially chosen temperatures and electron fractions in the tori to values that correspond to thermal and kinetic equilibrium

conditions. Except for a short period at the beginning of the merger-remnant simulations, the long-time evolution of the tori therefore mostly depends on the applied value of the α -viscosity and on the neutrino transport, and only to a minor degree on the exact initial conditions.

Consistent with previously published conformally flat (e.g., Oechslin et al. 2007; Goriely et al. 2011b; Bauswein et al. 2013b) and fully relativistic results (e.g., Hotokezaka et al. 2013a,b; Kyutoku et al. 2011, 2013; Deaton et al. 2013; Foucart et al. 2014; Wanajo et al. 2014), the “dynamical” ejecta of NS-NS and NS-BH mergers, which are expelled within milliseconds of the collision of the two binary components, were found to possess similar average properties, namely expansion velocities of 0.2–0.4 c , electron fractions below ~ 0.1 , and entropies per baryon of a few k_B . The considered NS-NS mergers produce ~ 0.004 – $0.021 M_\odot$ of ejecta, whereas the NS-BH mergers eject significantly larger masses, 0.035–0.08 M_\odot , with very low entropies ($\lesssim 1 k_B$ per nucleon), because this matter is not shock heated as in NS-NS collisions, but originates mostly from the outer tail of the tidally stretched NS at its final approach to the BH. Mass lost in NS-BH mergers is also expelled much more asymmetrically than in the case of NS-NS mergers: Corresponding hemispheric asymmetry parameters (mass difference between dominant ejecta hemisphere and opposite hemisphere, divided by total ejecta mass) are a few per cent for symmetric NS-NS mergers and 15–30% for strongly asymmetric ones, but 0.93–0.98 for NS-BH mergers.

Since the high neutron excess, thermodynamic properties, and expansion timescale are very similar, the ejecta of NS-NS mergers as well as those of NS-BH mergers are sites of robust production of r-nuclei with $A \gtrsim 140$ and abundances close to the solar distribution. This result holds basically independently of the considered nuclear EOS and the exact binary parameters and confirms the findings of previous studies based on different kinds of relativistic merger simulations (e.g., Goriely et al. 2011b; Bauswein et al. 2013b; Hotokezaka et al. 2013a; Wanajo et al. 2014).

The relic BH-torus systems lose mass in neutrino-driven baryonic winds (e.g., Wanajo & Janka 2012) and in outflows triggered by viscous energy dissipation and angular momentum transport (e.g., Fernández & Metzger 2013). For the first time we quantitatively investigated these outflows by self-consistent simulations of the accretion-torus evolution with multi-dimensional, energy dependent neutrino transport. We found that the viscously driven ejecta amount up to, fairly model independent, 19–26% of the initial torus mass (for our BH spins of $A_{\text{BH}} = 0.8$) and dominate the neutrino-driven ejecta by far. The neutrino-driven wind depends extremely sensitively on the BH mass and on the torus mass, which determines the neutrino luminosities. The neutrino energy loss rates can reach several $10^{52} \text{ erg s}^{-1}$ up to more than $10^{53} \text{ erg s}^{-1}$ for each of ν_e and $\bar{\nu}_e$ for a few 100 ms. The neutrino-driven ejecta carry away up to about one per cent of the initial torus mass, but their mass can also be orders of magnitude lower. The maximum masses that can be associated with ejecta driven by neutrino heating are 2.5– $3.5 \times 10^{-3} M_\odot$ in the case of high neutrino luminosities for typical durations of fractions of a second up to ~ 1 s. This number agrees with the lower limit of the expelled mass computed by Perego et al. (2014) for a hypermassive NS as merger remnant, and the corresponding mass-loss rate

is roughly compatible with the values obtained for neutrino winds of proto-neutron stars in supernova cores (e.g., Qian & Woosley 1996). Neutrino heating, however, inflates the outer layers of the torus and has a positive feedback on the viscously driven mass ejection on the level of several per cent of the torus mass (or up to $\sim 20\%$ of the viscous-outflow mass).

Neutrino-driven torus winds exhibit characteristic properties which distinguish them from the viscously triggered outflow, namely the tendency of higher mean entropies, higher electron fractions, and larger expansion velocities (see Figs. 7, 9). Moreover, the neutrino wind is strongest at early times and at intermediate latitudes (around 45° away from the equatorial plane), and the entropy, electron fraction, and velocity exhibit a strong pole-to-equator variation with higher values towards the poles (Fig. 8). In contrast, viscously driven ejecta develop on longer timescales, are more spherical, and their properties vary little with angular direction.

Because of their greater neutron excess, viscously-driven ejecta allow for a much stronger r-process than the neutrino wind. The combination of both components is far dominated by the viscous contribution and matches the solar abundance pattern for all nuclear mass numbers $A \gtrsim 90$ fairly well. The abundance pattern for $A \leq 132$ is comparatively uniform, but the strength of the third abundance peak decreases with higher BH mass (Fig. 15), and the relative yields of low-mass ($A \lesssim 130$) and high-mass ($A \gtrsim 130$) components depend on the value of the dynamic viscosity and the detailed treatment of the viscosity terms in the hydrodynamics equations (Fig. 16).

A mass-weighted combination of the dynamical ejecta from the binary merger phase and the secular ejecta from the BH-torus evolution can reproduce the solar r-abundance pattern and therefore also that seen in ultra-metal-poor stars amazingly well in the range $90 \lesssim A < 240$ (cf. Figs. 19, 20). In particular, the BH-torus outflows are able to well fill the region $A \lesssim 140$, where the prompt merger ejecta underproduce the nuclei. Since the relative yields of the relic BH-torus systems for $A \lesssim 130$ and $A \gtrsim 130$ nuclei depend sensitively on the system parameters, whereas the $A \gtrsim 140$ species are created with a robust pattern during the binary merging phase, we expect a larger variability in the low- A regime than for high mass numbers (see Fig. 19).

Another interesting possibility is connected to the fact that the mass ejection during NS-BH mergers shows extreme spatial asymmetry (corresponding to asymmetry parameters $\gtrsim 0.95$) but the mass loss from their BH-torus remnants is much more isotropic. This can lead to a strong suppression of the dynamical ejecta component relative to the torus outflow in observer directions pointing away from the hemisphere that receives most of the expelled matter of the disrupted NS. Essentially pure BH-torus ejecta of some of our models can reasonably well match the abundance distributions observed in heavy-element deficient metal-poor stars like HD88609 and HD122563 (Fig. 21).

Since the major part of the torus ejecta ends up in forming $A \lesssim 130$ material, the additional mass loss of the merger remnants does not alter event-rate estimates based on comparing yields of heavy r-nuclei in the ejecta of the binary-merger phase with the r-process abundances in our Galaxy (e.g. Goriely et al. 2011b; Bauswein et al. 2014).

Regarding the sensitivity of the nucleosynthesis predic-

tions with respect to the nuclear physics input, we considered, in addition to the most recent data available experimentally, the latest theoretical rates based as much as possible on microscopic or semi-microscopic nuclear models (Xu et al. 2013). Such models have been shown to be able to compete with more phenomenological models as far as the accuracy in reproducing experimental data is concerned, and additionally are believed to be more predictive for exotic neutron-rich nuclei. Nevertheless, for such exotic nuclei, significant uncertainties still affect the prediction of the reaction and decay rates, as well as the fission fragment distributions (Arnould et al. 2007; Goriely et al. 2013, 2014; Goriely & Capote 2014). While we already partly investigated the sensitivity of the nucleosynthesis in the dynamical ejecta to masses, neutron capture rates, β -decay rates, and fission probabilities (Goriely et al. 2013, 2014; Xu et al. 2014), a detailed sensitivity analysis for the composition of the disk ejecta from the BH-torus systems remains to be performed in the future. Nuclear physics uncertainties may affect the calculated abundance distributions, and more specifically, the precise location and width of the second ($A \sim 130$), rare-earth ($A \sim 165$) and third ($A \sim 195$) peaks, but should not change the overall nucleosynthesis picture, and especially not the successful r-process production of $A \gtrsim 90$ nuclei.

Our work can represent only a beginning of the combined analysis of binary merger and post-merger ejecta concerning their nucleosynthetic impact. The parameter space of system properties (masses, mass ratios, BH spin values and orientations) and internal properties (defined by the uncertain nuclear EOS of NS matter) is huge and the involved physics is extremely complex and not fully accounted for in our simulations.

The merger and remnant models employed in our study are still incomplete in many respects. Instead of simulating the merger phase and remnant evolution consistently and continuously with the same numerics in full 3D general relativity, we applied different codes and approximations for these two evolutionary periods. Neutrino transport was only included for the BH-torus simulations, but we ignored neutrino effects during the merger phase. Neutrinos are unlikely to have a strong influence in cases where NS-NS merger remnants collapse to a BH immediately and matter is ejected only on very short timescales, and they do not play an important role in NS-BH mergers, where the material ejected from the disrupted NS is never shock heated. However, Wanajo et al. (2014) pointed out that the neutrino emission and reabsorption could well have an impact on the electron fraction of NS-NS merger ejecta for long(er)-lived massive NS-merger remnants, in particular for soft NS EOSs. Neutrino oscillations and general relativistic effects (both ignored in our Newtonian torus models) were found to be of relevance for an exact determination of the neutron-to-proton ratio in neutrino-driven disk winds (e.g., Malkus et al. 2012; Caballero et al. 2012). However, these complications may not be overly relevant because neutrino-driven ejecta are dwarfed in mass by the viscous outflows, which are expelled at large distances from the central BH and whose electron fraction is governed by electron and positron captures rather than neutrino captures. The low Y_e of this clearly dominant torus-ejecta component also lowers the perspective of significant nickel production (Surman et al. 2014) in these outflows.

The application of a viscosity description instead of magnetohydrodynamic modeling is a major source of uncertainty, whose consequences may well influence the nucleosynthetic predictions, as we have shown. A reliable numerical description of the mechanism that drives turbulent angular momentum transport and ultimately gives rise to the (quasi-) viscous ejecta encountered for post-merger BH-tori is beyond the scope of the present study. The α -viscosity treatment employed here is a computationally pragmatic approach that efficiently circumvents the task of numerically modeling turbulent, magnetized disks. The evolution of magnetized accretion disks is an active field of research on its own with several fundamental issues being still vividly debated, e.g., numerical convergence (e.g. Fromang & Papaloizou 2007; Hawley et al. 2013; Sorathia et al. 2012), impact of the global magnetic-field topology (e.g. Beckwith et al. 2008), or the relevance of additional instabilities besides the magnetorotational instability (MRI) (e.g. Narayan et al. 2012; Yuan et al. 2012). Nevertheless, although all of the aforementioned issues may have implications for the disk-outflow masses and the evolution of a given configuration, it seems likely that the principal result of our study is robust, namely that a significant fraction of order 10% or more of the accretion torus become unbound with sufficiently neutron-rich conditions to allow for the formation of r-process elements with $90 \lesssim A \lesssim 140$.

Our work explicitly excludes long-lived hypermassive or supermassive NSs as merger remnants, whose disk mass loss was recently studied by Metzger & Fernández (2014) and Perego et al. (2014). Both groups replaced the core of the massive remnant by an inner boundary condition. Such stable objects might be common relics of approximately symmetric NS-NS mergers with typical NS masses of ~ 1.35 – $1.45 M_\odot$ for EOSs that are consistent with the observed $\sim 2 M_\odot$ lower limit of the maximum mass of nonrotating, cold NSs (Demorest et al. 2010; Antoniadis et al. 2013). Fully self-consistent simulations will not only have to involve highly differential rotation and convection and the associated amplification of magnetic fields to extreme strengths in a nuclear environment with high sound and Alfvén speeds, but it will also encounter all the complexities of the high-density nuclear and neutrino physics that complicate long-time evolution calculations of neutrino-cooling proto-neutron stars in supernovae. This ambitious undertaking is deferred to future work.

ACKNOWLEDGMENTS

OJ wishes to thank Martin Obergaulinger, Bernhard Müller and Reiner Birkel for helpful discussions. At Garching, this research was supported by the Max-Planck/Princeton Center for Plasma Physics (MPPC) and by the Deutsche Forschungsgemeinschaft through the Transregional Collaborative Research Center SFB/TR 7 “Gravitational Wave Astronomy” and the Cluster of Excellence EXC 153 “Origin and Structure of the Universe” (<http://www.universe-cluster.de>). AB is a Marie Curie Intra-European Fellow within the 7th European Community Framework Programme (IEF 331873). SG acknowledges financial support from FNRS (Belgium). We are also grateful for computational support by the Center for Computational Astro-

physics (C2PAP) at the Leibniz Rechenzentrum (LRZ) and by the Rechenzentrum Garching (RZG).

REFERENCES

- Aloy M. A., Janka H., Müller E., 2005, *A&A*, 436, 273
- Antoniadis J., et al., 2013, *Science*, 340, 448
- Arcones A., Martínez-Pinedo G., Roberts L. F., Woosley S. E., 2010, *A&A*, 522, A25+
- Arnould M., Goriely S., Takahashi K., 2007, *Phys. Rep.*, 450, 97
- Artemova I. V., Bjoernsson G., Novikov I. D., 1996, *ApJ*, 461, 565
- Audit E., Charrier P., Chièze J. ., Dubroca B., 2002, preprint ([arXiv:astro-ph/0206281](https://arxiv.org/abs/astro-ph/0206281))
- Bardeen J. M., Press W. H., Teukolsky S. A., 1972, *ApJ*, 178, 347
- Barnes J., Kasen D., 2013, *ApJ*, 775, 18
- Baumgarte T. W., Shapiro S. L., 2010, *Numerical relativity: Solving Einstein's Equations on the Computer*. Cambridge University Press, Cambridge
- Baumgarte T. W., Shapiro S. L., Shibata M., 2000, *ApJL*, 528, L29
- Bauswein A., 2010. PhD thesis, Technical University Munich
- Bauswein A., Janka H.-T., Oechslin R., 2010, *Phys. Rev. D*, 82, 084043
- Bauswein A., Janka H.-T., Hebel K., Schwenk A., 2012, *Phys. Rev. D*, 86, 063001
- Bauswein A., Baumgarte T. W., Janka H.-T., 2013a, *Physical Review Letters*, 111, 131101
- Bauswein A., Goriely S., Janka H.-T., 2013b, *ApJ*, 773, 78
- Bauswein A., Ardevol Pulpillo R., Janka H.-T., Goriely S., 2014, *ApJL*, 795, L9
- Beckwith K., Hawley J. F., Krolik J. H., 2008, *ApJ*, 678, 1180
- Belczynski K., Kalogera V., Rasio F. A., Taam R. E., Zezas A., Bulik T., Maccarone T. J., Ivanova N., 2008, *ApJS*, 174, 223
- Beloborodov A. M., 2003, *ApJ*, 588, 931
- Beloborodov A. M., 2008, in Axelsson M., ed., *AIP Conf. Ser. Vol. 1054, Hyper-accreting black holes*. pp 51–70
- Berger E., 2014, *ARA& A*, 52, 43
- Berger E., Fong W., Chornock R., 2013, *ApJL*, 774, L23
- Bildsten L., Cutler C., 1992, *ApJ*, 400, 175
- Birkel R., Aloy M. A., Janka H.-T., Müller E., 2007, *A&A*, 463, 51
- Bonazzola S., Gourgoulhon E., Grandclément P., Novak J., 2004, *Phys. Rev. D*, 70, 104007
- Bowen J. M., 1979, *General Relativity and Gravitation*, 11, 227
- Bowen J. M., York Jr. J. W., 1980, *Phys. Rev. D*, 21, 2047
- Brandt S., Brüggmann B., 1997, *Phys. Rev. Lett.*, 78, 3606
- Bruenn S. W., 1985, *ApJS*, 58, 771
- Caballero O. L., McLaughlin G. C., Surman R., 2012, *ApJ*, 745, 170
- Chen W., Beloborodov A. M., 2007, *ApJ*, 657, 383
- Cooperstein J., van den Horn L. J., Baron E., 1987, *ApJL*, 321, L129
- Cordero-Carrión I., Cerdá-Durán P., Dimmelmeier H., Jaramillo J. L., Novak J., Gourgoulhon E., 2009, *Phys. Rev. D*, 79, 024017
- Deaton M. B., et al., 2013, *ApJ*, 776, 47
- Demorest P. B., Pennucci T., Ransom S. M., Roberts M. S. E., Hessels J. W. T., 2010, *Nature*, 467, 1081
- Dessart L., Ott C. D., Burrows A., Rosswog S., Livne E., 2009, *ApJ*, 690, 1681
- Di Matteo T., Perna R., Narayan R., 2002, *ApJ*, 579, 706
- Dicus D. A., 1972, *Phys. Rev. D*, 6, 941
- Dominik M., Belczynski K., Fryer C., Holz D. E., Berti E., Bulik T., Mandel I., O'Shaughnessy R., 2012, *ApJ*, 759, 52
- Eichler D., Livio M., Piran T., Schramm D. N., 1989, *Nature*, 340, 126
- Etienne Z. B., Liu Y. T., Shapiro S. L., Baumgarte T. W., 2009, *Phys. Rev. D*, 79, 044024
- Faber J. A., Baumgarte T. W., Shapiro S. L., Taniguchi K., Rasio F. A., 2006, *Phys. Rev. D*, 73, 024012
- Fernández R., Metzger B. D., 2013, *MNRAS*, 435, 502
- Foucart F., et al., 2014, *Phys. Rev. D*, 90, 024026
- Freiburghaus C., Rosswog S., Thielemann F.-K., 1999, *ApJL*, 525, L121
- Fromang S., Papaloizou J., 2007, *A&A*, 476, 1113
- Goriely S., 1999, *A&A*, 342, 881
- Goriely S., Capote R., 2014, *Phys. Rev. C*, 89, 054318
- Goriely S., Demetriou P., Janka H., Pearson J. M., Samyn M., 2005, *Nuclear Physics A*, 758, 587
- Goriely S., Samyn M., Pearson J. M., 2007, *Phys. Rev. C*, 75, 064312
- Goriely S., Hilaire S., Koning A. J., 2008, *A&A*, 487, 767
- Goriely S., Hilaire S., Koning A. J., Sin M., Capote R., 2009, *Phys. Rev. C*, 79, 024612
- Goriely S., Chamel N., Pearson J. M., 2010, *Phys. Rev. C*, 82, 035804
- Goriely S., Chamel N., Janka H.-T., Pearson J. M., 2011a, *A&A*, 531, A78
- Goriely S., Bauswein A., Janka H.-T., 2011b, *ApJL*, 738, L32+
- Goriely S., Sida J.-L., Lemaître J.-F., Panebianco S., Dubray N., Hilaire S., Bauswein A., Janka H.-T., 2013, *Physical Review Letters*, 111, 242502
- Goriely S., Bauswein A., Janka H.-T., Sida J.-L., Lemaître J.-F., Panebianco S., Dubray N., Hilaire S., 2014, in Jeong S., Imai N., Miyatake H., Kajino T., eds, *AIP Conf. Ser. Vol. 1594*, pp 357–364
- Grossman D., Korobkin O., Rosswog S., Piran T., 2014, *MNRAS*, 439, 757
- Harikae S., Kotake K., Takiwaki T., Sekiguchi Y.-i., 2010, *ApJ*, 720, 614
- Hawley J. F., Richers S. A., Guan X., Krolik J. H., 2013, *ApJ*, 772, 102
- Hempel M., Schaffner-Bielich J., 2010, *Nucl. Phys. A*, 837, 210
- Hempel M., Fischer T., Schaffner-Bielich J., Liebendörfer M., 2012, *ApJ*, 748, 70
- Honda S., Aoki W., Ishimaru Y., Wanajo S., 2007, *ApJ*, 666, 1189
- Hotkezaka K., Kiuchi K., Kyutoku K., Okawa H., Sekiguchi Y.-i., Shibata M., Taniguchi K., 2013a, *Phys. Rev. D*, 87, 024001
- Hotkezaka K., Kyutoku K., Tanaka M., Kiuchi K.,

- Sekiguchi Y., Shibata M., Wanajo S., 2013b, *ApJL*, 778, L16
- Igumenshchev I. V., Abramowicz M. A., 1999, *MNRAS*, 303, 309
- Igumenshchev I. V., Chen X., Abramowicz M. A., 1996, *MNRAS*, 278, 236
- Isenberg J., Nester J., 1980, in Held A., ed., *General Relativity and Gravitation. Vol. 1. One hundred years after the birth of Albert Einstein*, NY: Plenum Press, p. 23
- Janiuk A., Mioduszewski P., Moscibrodzka M., 2013, *ApJ*, 776, 105
- Janka H.-T., Ruffert M., 2002, in Shara M. M., ed., *Astronomical Society of the Pacific Conference Series Vol. 263, Stellar Collisions, Mergers and their Consequences*. p. 333
- Janka H.-T., Eberl T., Ruffert M., Fryer C. L., 1999, *ApJL*, 527, L39
- Jaroszynski M., 1993, *Acta Astronomica*, 43, 183
- Kalogera V., et al., 2004, *ApJL*, 601, L179
- Kasen D., Badnell N. R., Barnes J., 2013, *ApJ*, 774, 25
- Kochanek C. S., 1992, *ApJ*, 398, 234
- Kodama T., Takahashi K., 1975, *Nuclear Physics A*, 239, 489
- Kohri K., Mineshige S., 2002, *ApJ*, 577, 311
- Koning A. J., Hilaire S., Duijvestijn M. C., 2005, in Haight R. C., Chadwick M. B., Kawano T., Talou P., eds, *AIP Conf. Ser. Vol. 769, International Conference on Nuclear Data for Science and Technology*. pp 1154–1159
- Korobkin O., Rosswog S., Arcones A., Winteler C., 2012, *MNRAS*, 426, 1940
- Kulkarni S. R., 2005, preprint ([arXiv:astro-ph/0510256](https://arxiv.org/abs/astro-ph/0510256))
- Kyutoku K., Shibata M., Taniguchi K., 2009, *Phys. Rev. D*, 79, 124018
- Kyutoku K., Okawa H., Shibata M., Taniguchi K., 2011, *Phys. Rev. D*, 84, 064018
- Kyutoku K., Ioka K., Shibata M., 2013, *Phys. Rev. D*, 88, 041503
- Lattimer J. M., 2012, *Annual Review of Nuclear and Particle Science*, 62, 485
- Lattimer J. M., Schramm D. N., 1974, *ApJL*, 192, L145
- Lattimer J. M., Schramm D. N., 1976, *ApJ*, 210, 549
- Lee W. H., Ramirez-Ruiz E., Page D., 2005, *ApJ*, 632, 421
- Li L.-X., Paczyński B., 1998, *ApJL*, 507, L59
- Malkus A., Kneller J. P., McLaughlin G. C., Surman R., 2012, *Phys. Rev. D*, 86, 085015
- Malkus A., Friedland A., McLaughlin G. C., 2014, preprint ([arXiv:1403.5797](https://arxiv.org/abs/1403.5797))
- Metzger B. D., Berger E., 2012, *ApJ*, 746, 48
- Metzger B. D., Fernández R., 2014, *MNRAS*, 441, 3444
- Metzger B. D., Piro A. L., Quataert E., 2008, *MNRAS*, 390, 781
- Metzger B. D., Piro A. L., Quataert E., 2009, *MNRAS*, 396, 304
- Metzger B. D., et al., 2010, *MNRAS*, 406, 2650
- Meyer B. S., 1989, *ApJ*, 343, 254
- Minerbo G. N., 1978, *J. Quant. Spec. Radiat. Transf.*, 20, 541
- Nakar E., 2007, *Phys. Rep.*, 442, 166
- Narayan R., Yi I., 1994, *ApJL*, 428, L13
- Narayan R., Sadowski A., Penna R. F., Kulkarni A. K., 2012, *MNRAS*, 426, 3241
- O'Connor E., Ott C. D., 2013, *ApJ*, 762, 126
- Obergaulinger M., 2008, PhD thesis, Technical University Munich
- Oechslin R., Rosswog S., Thielemann F.-K., 2002, *Phys. Rev. D*, 65, 103005
- Oechslin R., Janka H., Marek A., 2007, *A&A*, 467, 395
- Paczynski B., 1986, *ApJL*, 308, L43
- Paczyński B., Wiita P. J., 1980, *A&A*, 88, 23
- Panebianco S., Sida J.-L., Goutte H., Lemaître J.-F., Dubray N., Hilaire S., 2012, *Phys. Rev. C*, 86, 064601
- Perego A., Rosswog S., Cabezón R. M., Korobkin O., Käppeli R., Arcones A., Liebendörfer M., 2014, *MNRAS*, 443, 3134
- Popham R., Woosley S. E., Fryer C., 1999, *ApJ*, 518, 356
- Postnov K. A., Yungelson L. R., 2014, *Living Reviews in Relativity*, 17, 3
- Price D. J., 2007, *PASA*, 24, 159
- Qian Y., Woosley S. E., 1996, *ApJ*, 471, 331
- Roberts L. F., Kasen D., Lee W. H., Ramirez-Ruiz E., 2011, *ApJL*, 736, L21+
- Roederer I. U., 2011, *ApJL*, 732, L17
- Roederer I. U., Cowan J. J., Karakas A. I., Kratz K.-L., Lugaro M., Simmerer J., Farouqi K., Sneden C., 2010, *ApJ*, 724, 975
- Rosswog S., 2005, *ApJ*, 634, 1202
- Rosswog S., Liebendörfer M., Thielemann F.-K., Davies M. B., Benz W., Piran T., 1999, *A&A*, 341, 499
- Rosswog S., Korobkin O., Arcones A., Thielemann F.-K., Piran T., 2014, *MNRAS*, 439, 744
- Ruffert M., Janka H.-T., 1999, *A&A*, 344, 573
- Ruffert M., Janka H.-T., 2001, *A&A*, 380, 544
- Ruffert M., Janka H.-T., Takahashi K., Schaefer G., 1997, *A&A*, 319, 122
- Sądowski A., Narayan R., Tchekhovskoy A., Zhu Y., 2013, *MNRAS*, 429, 3533
- Schinder P. J., Schramm D. N., Wiita P. J., Margolis S. H., Tubbs D. L., 1987, *ApJ*, 313, 531
- Setiawan S., Ruffert M., Janka H.-T., 2004, *MNRAS*, 352, 753
- Setiawan S., Ruffert M., Janka H.-T., 2006, *A&A*, 458, 553
- Shakura N. I., Sunyaev R. A., 1973, *A&A*, 24, 337
- Shibata M., Sekiguchi Y., 2012, *Progress of Theoretical Physics*, 127, 535
- Shibata M., Sekiguchi Y., Takahashi R., 2007, *Progress of Theoretical Physics*, 118, 257
- Shibata M., Kiuchi K., Sekiguchi Y., Suwa Y., 2011, *Progress of Theoretical Physics*, 125, 1255
- Siegel D. M., Ciolfi R., Rezzolla L., 2014, *ApJL*, 785, L6
- Siegler S., Riffert H., 2000, *ApJ*, 531, 1053
- Skinner M. A., Ostriker E. C., 2013, *ApJS*, 206, 21
- Sneden C., et al., 2003, *ApJ*, 591, 936
- Sneden C., Cowan J. J., Gallino R., 2008, *ARA&A*, 46, 241
- Sneden C., Lawler J. E., Cowan J. J., Ivans I. I., Den Hartog E. A., 2009, *ApJS*, 182, 80
- Sorathia K. A., Reynolds C. S., Stone J. M., Beckwith K., 2012, *ApJ*, 749, 189
- Steiner A. W., Hempel M., Fischer T., 2013, *ApJ*, 774, 17
- Stone J. M., Pringle J. E., Begelman M. C., 1999, *MNRAS*, 310, 1002
- Sugahara Y., Toki H., 1994, *Nucl. Phys. A*, 579, 557
- Surman R., McLaughlin G. C., Ruffert M., Janka H.-T., Hix W. R., 2008, *ApJL*, 679, L117
- Surman R., Caballero O. L., McLaughlin G. C., Just O.,

- Janka H.-T., 2014, *Journal of Physics G Nuclear Physics*, 41, 044006
- Tachibana T., Yamada M., Yoshida Y., 1990, *Progress of Theoretical Physics*, 84, 641
- Takami K., Rezzolla L., Baiotti L., 2014, *Physical Review Letters*, 113, 091104
- Tanaka M., Hotokezaka K., 2013, *ApJ*, 775, 113
- Tanaka M., Hotokezaka K., Kyutoku K., Wanajo S., Kiuchi K., Sekiguchi Y., Shibata M., 2014, *ApJ*, 780, 31
- Tanvir N. R., Levan A. J., Fruchter A. S., Hjorth J., Hounsell R. A., Wiersema K., Tunnicliffe R. L., 2013, *Nature*, 500, 547
- Tejeda E., Rosswog S., 2013, *MNRAS*, 433, 1930
- Toki H., Hirata D., Sugahara Y., Sumiyoshi K., Tanihata I., 1995, *Nucl. Phys. A*, 588, 357
- Typel S., Röpke G., Klähn T., Blaschke D., Wolter H. H., 2010, *Phys. Rev. C*, 81, 015803
- Wanajo S., Janka H.-T., 2012, *ApJ*, 746, 180
- Wanajo S., Sekiguchi Y., Nishimura N., Kiuchi K., Kyutoku K., Shibata M., 2014, *ApJL*, 789, L39
- Wilson J. R., Mathews G. J., Marronetti P., 1996, *Phys. Rev. D*, 54, 1317
- Xu Y., Goriely S., Jorissen A., Chen G. L., Arnould M., 2013, *A&A*, 549, A106
- Xu Y., Goriely S., Koning A. J., Hilaire S., 2014, *Phys. Rev. C*, 90, 024604
- Yuan F., Bu D., Wu M., 2012, *ApJ*, 761, 130

APPENDIX A: NEUTRINO FIELD AROUND A TORUS

In order to assess the quality of the approximate neutrino-transport scheme used for the BH-torus simulations in this paper – denoted as AEF (algebraic-Eddington-factor) scheme hereafter – we present here some results of a comparison between the AEF scheme and an accurate radiative transfer solver. For a detailed description of the AEF scheme, its implementation, and various additional tests, we refer the reader to a forthcoming paper (Just et al., in preparation).

The hydrodynamic configuration is essentially given by the state of model M3A8m3a5 at evolution time $t = 50$ ms (cf. Panels (a) and (b) of Fig. 5 for contour plots of some thermodynamic quantities). However, for this test, we only evolve the neutrino radiation field while keeping all hydrodynamic quantities fixed. Moreover, to facilitate the comparison with the reference neutrino scheme (see next paragraph) we now ignore frame-dependent effects in the neutrino scheme, i.e. all velocities are set to zero, and for the neutrino interactions we only include emission and absorption by nucleons.

To judge the results of the AEF method, a reference calculation is conducted with a more accurate (but also computationally far more expensive) neutrino scheme, namely a ray-tracing method (RT hereafter). In the RT method, the time-independent Boltzmann equation,

$$\mathbf{n} \cdot \nabla f(\mathbf{x}, \mathbf{n}) = \kappa_a(\mathbf{x}) [(f^0(\mathbf{x}) - f(\mathbf{x}, \mathbf{n}))], \quad (\text{A1})$$

(where \mathbf{x} and \mathbf{n} are the spatial coordinate vector and the neutrino-momentum unit vector, respectively) is solved for the distribution function $f(\mathbf{x}, \mathbf{n})$ by direct integration along

straight rays directed towards \mathbf{n} , given the absorption opacity $\kappa_a(\mathbf{x})$ and the Fermi distribution function $f^0(\mathbf{x})$ (see, e.g., Birkel et al. 2007 and Harikae et al. 2010 for related approaches in the context of neutrino transfer). In practice, for each species, energy group and spatial grid point we integrate Eq. (A1) along $\sim 60\,000$ ray directions, corresponding to an angular resolution of $\approx 1^\circ$. We checked that all relevant quantities are numerically converged to better than $\sim 1\%$ with respect to the number of rays and the step size used for integration of Eq. (A1). The spatial and energy grids are identical in both calculations and directly adopted from the time-dependent simulation (cf. Sect. 2.2), except that the radial domain is now restricted to radii $r \lesssim 500$ km (corresponding to ~ 250 radial grid points).

In Fig. A1 we summarize the results of both calculations. A satisfactory outcome is the fact that the luminosities with $\{L_{\nu_e}, L_{\bar{\nu}_e}\}_{\text{RT}} = \{4.88, 7.13\} \times 10^{52} \text{ erg s}^{-1}$ and $\{L_{\nu_e}, L_{\bar{\nu}_e}\}_{\text{AEF}} = \{5.93, 8.25\} \times 10^{52} \text{ erg s}^{-1}$, as well as the mean energies with $\{\varepsilon_{\nu_e}, \varepsilon_{\bar{\nu}_e}\}_{\text{RT}} = \{14.0, 17.2\} \text{ MeV}$ and $\{\varepsilon_{\nu_e}, \varepsilon_{\bar{\nu}_e}\}_{\text{AEF}} = \{14.6, 17.8\} \text{ MeV}$ (cf. Fig. A1, Panels (a), (b), (d) and (e)) agree fairly well, with the AEF quantities all being shifted by at most $\sim 20\%$ towards higher values compared to the corresponding RT results. Also, the local distributions of the energy-integrated energy density, E , and flux density, F , (compared in Panels (a)–(f) of Fig. A1 for electron neutrinos) agree quite well in the bulk of the torus and close to the equator.

However, the agreement of the local neutrino distribution is not everywhere perfect. For directions closer to the polar axis the neutrino density obtained by the AEF method appears to be overestimated by factors of up to ~ 2 – 3 while being underestimated by up to few tens of percent between the polar region and the equatorial plane. This feature might be the consequence of the constrained ability of AEF schemes to correctly describe the superposition of oblique radiation fronts (see, e.g., Skinner & Ostriker 2013; Sądowski et al. 2013 for more comments on this property, which is closely related to what is sometimes called “two-beam instability”). From the mathematical point of view, this shortcoming can be understood from the fact that the moment equations in the AEF formulation are non-linear, even in the optically thin limit, owing to the generally non-linear closure relation for the Eddington factor, whereas the original Boltzmann equation is linear. In our case of a radiating torus, neutrino beams that stem from different locations on the torus surface and that should cross each other without interaction are instead slightly deflected into the radial direction, thereby causing an artificial enhancement of the neutrino density around the polar axis and, in turn, a corresponding shortage of neutrinos propagating along their original directions pointing away from the axis.

As can be inferred from Panels (g) and (i) of Fig. A1, the net neutrino heating and cooling rates, Q_ν , show good agreement inside the torus and near the equatorial plane but an enhancement in the polar region compared to the corresponding RT result, very similar to the behavior of E . In Panels (h) and (j) of Fig. A1 we show the electron fraction corresponding to local neutrino-capture equilibrium, Y_e^ν , which is approximately computed as $Y_e^\nu \approx [1 + E_{\bar{\nu}_e}/E_{\nu_e} \times (\varepsilon_{4,\bar{\nu}_e} - 2Q_{\text{np}})/(\varepsilon_{4,\nu_e} + 2Q_{\text{np}})]^{-1}$ where Q_{np} is the mass difference between neutrons and protons and $\varepsilon_{4,\nu_e} \equiv \int \int \epsilon_{\nu_e}^4 f d\Omega d\epsilon_{\nu_e} / \int \int \epsilon_{\nu_e}^3 f d\Omega d\epsilon_{\nu_e}$ with the neutrino en-

Neutrino Field Around Torus

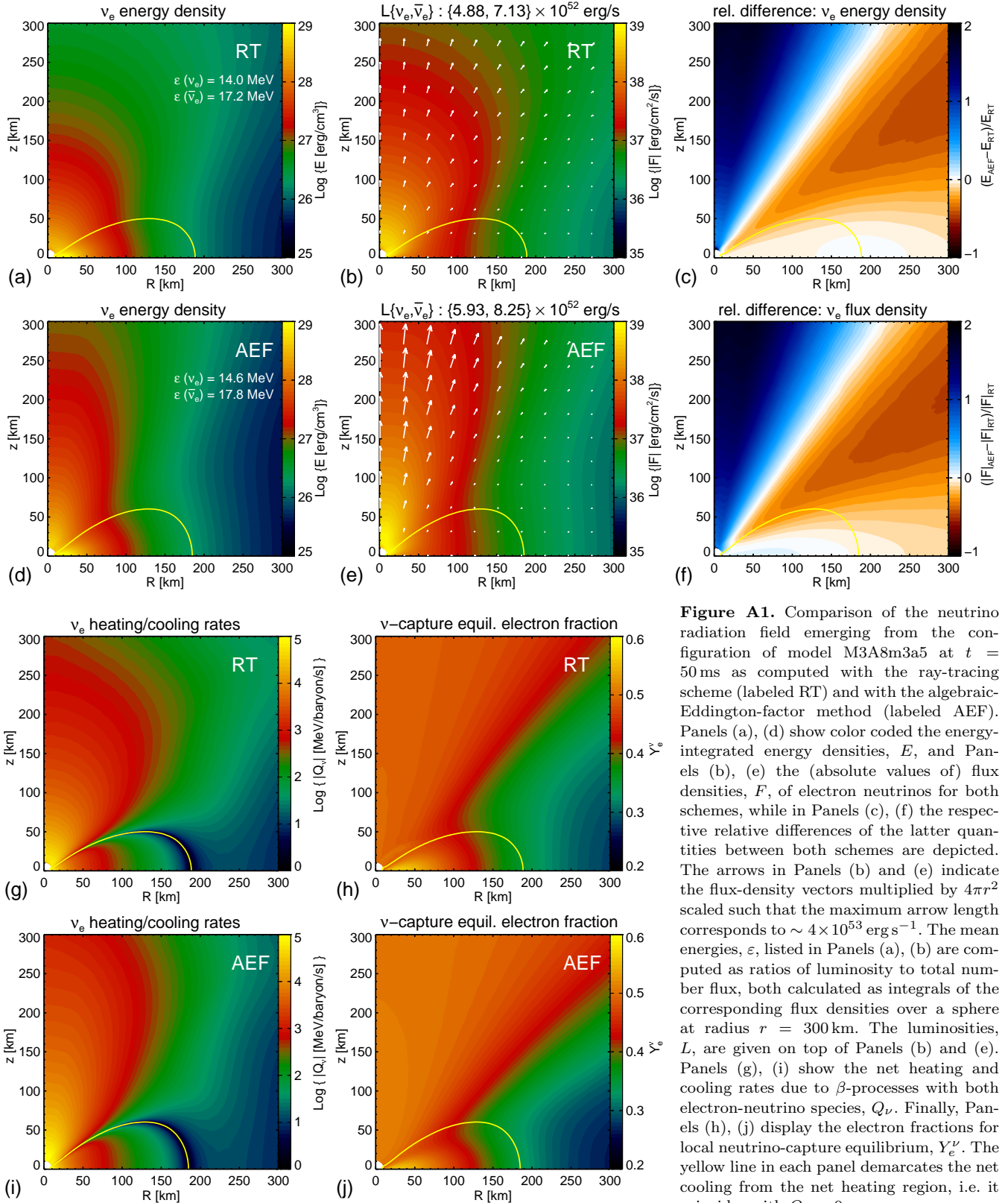


Figure A1. Comparison of the neutrino radiation field emerging from the configuration of model M3A8m3a5 at $t = 50$ ms as computed with the ray-tracing scheme (labeled RT) and with the algebraic-Eddington-factor method (labeled AEF). Panels (a), (d) show color coded the energy-integrated energy densities, E , and Panels (b), (e) the (absolute values of) flux densities, F , of electron neutrinos for both schemes, while in Panels (c), (f) the respective relative differences of the latter quantities between both schemes are depicted. The arrows in Panels (b) and (e) indicate the flux-density vectors multiplied by $4\pi r^2$ scaled such that the maximum arrow length corresponds to $\sim 4 \times 10^{53}$ erg s $^{-1}$. The mean energies, ϵ , listed in Panels (a), (b) are computed as ratios of luminosity to total number flux, both calculated as integrals of the corresponding flux densities over a sphere at radius $r = 300$ km. The luminosities, L , are given on top of Panels (b) and (e). Panels (g), (i) show the net heating and cooling rates due to β -processes with both electron-neutrino species, Q_ν . Finally, Panels (h), (j) display the electron fractions for local neutrino-capture equilibrium, Y_e^ν . The yellow line in each panel demarcates the net cooling from the net heating region, i.e. it coincides with $Q_\nu = 0$.

ergy ϵ_ν and momentum-space solid angle Ω . In contrast to the heating rates, Y_e^ν only exhibits deviations of up to $\sim 10 - 20\%$ between both calculations, which is due to the fact that this quantity mostly depends on the ratio of the ν_e and $\bar{\nu}_e$ energy densities and not on their individual values. Owing to the fact that the spatial emission characteristics of $\bar{\nu}_e$ are very similar to those of ν_e in both cases, RT and AEF, the energy ratios match rather closely between both calculations.

The test results are encouraging concerning the main conclusions drawn in this paper. Assuming the setup is representative for all models investigated in our main study, the above results would suggest that the global neutrino-emission properties and therefore the cooling and (de-)leptonization behavior of the bulk of the torus are probably captured rather accurately. Consequently, it could then be assumed that the conditions leading into the ADAF phase and to the development of the viscous outflow are described properly. Therefore, the properties and nucleosynthesis signature of the dominant outflow component and, hence, the main conclusions drawn in this paper, should be fairly robust with respect to the neutrino scheme. The deposition of energy and lepton-number by neutrinos in the surface layers of the torus might be systematically overestimated due to the artificial overabundance of neutrinos near the axis region. This could imply that the neutrino-driven wind masses, which are already small compared to the viscous outflow masses, are even overestimated in our study. In contrast, the nucleosynthesis properties of the neutrino-driven ejecta are likely to be robust because the electron fractions are driven towards high asymptotic values of $Y_e^\nu \sim 0.4 - 0.5$ also in the RT case. However, since this test only examines a single static torus configuration using simplified neutrino interactions, we refrain from speculations about the quantitative error introduced by the approximations of the AEF scheme to the time-dependent BH-torus models considered in this paper. The quantitative difference to accurate neutrino transport in torus evolution models can ultimately only be revealed by comparing to neutrino-hydrodynamics simulations including a Boltzmann-type transport solver.